THESIS FOR THE DEGREE OF DOCTOR OF ENGINEERING

Development of a new generation of creep resistant 12% chromium steels:

Microstructure of Z-phase strengthened steels

Masoud Rashidi

CHALMERS
UNIVERSITY OF TECHNOLOGY

Department of Physics

CHALMERS UNIVERSITY OF TECHNOLOGY

Gothenburg, Sweden 2017

Development of a new generation of creep resistant 12% chromium steels:
Microstructure of Z-phase strengthened steels
Masoud Rashidi

ISBN 978-91-7597-649-5
Doktorsavhandlingar vid Chalmers tekniska högskola
Ny serie nr 4330
ISSN 0346-718X

Division of Materials Microstructure
Department of Physics
Chalmers University of Technology
SE-412 96 Gothenburg
Sweden
Telephone: +46 (0)31-772 3337

Cover images:

Top left: Atom probe tomography reconstruction of precipitates of Ta(C, N), a precursor phases to Z-phase, on a presumably lath boundary.

Top right: Transmission electron micrograph showing a fine distribution of Z-phase precipitates with blade-like morphology.

Bottom left: Transmission electron micrograph showing the beneficial effect of Z-phase in hindering dislocations and providing creep resistance.

Bottom right: Atom probe tomography reconstruction showing heterogeneous precipitation of $M_{23}C_6$ (Cr map), Cu, Z-phase (Ta+Nb map), and Laves-phase (W map) precipitates. In the investigated steels within the thesis, there are many phases that directly or indirectly affect or are affected by Z-phase precipitation and we need to consider all of them in alloy design.

Printed at Chalmers Reproservice
Gothenburg Sweden 2017

Dedicated to

My Family

Development of a new generation of creep resistant 12% chromium steels:
Microstructure of Z-phase strengthened steels

Masoud Rashidi
Department of Physics
Chalmers University of Technology

Abstract

Fossil-fuel fired steam power plants provide more than 60% of the electricity generated worldwide, and account for about one third of the global CO_2 emissions. Increasing the steam temperature and pressure leads to a higher thermal efficiency of the power plants and thus lower emissions. The efficiency is limited by the long-term corrosion and creep resistance of economically viable materials used in the critical components of such a power plant, 9–12% Cr steels. Increasing the Cr content from 9% to 11–12% in the best commercially available steels provides sufficient corrosion resistance for an increase from the current maximum steam temperature of 620°C to 650°C for future power plants. However, after a few years of service, formation of coarse Z-phase (Cr(Nb, V)N) precipitates at the expense of a fine distribution of VN precipitates degrades the precipitation hardening and accordingly creep resistance of the steels.

In this work a new family of 12% chromium steels is studied, where Ta or Nb is used instead of V to strengthen the steel by forming a dense distribution of Z-phase rather than VN. Z-phase does not nucleate directly as Z-phase, instead it forms through a gradual transformation of existing MX and M_2N precipitates. The former leads to the formation of Z-phase with a blade-like morphology and the latter promotes large bulky Z-phase precipitates. As a result of the MX to Z-phase transformation, creep strength comparable to commercially available 9% Cr steels can be achieved. Investigation on the Z-phase precipitates based on Ta or Nb showed that Ta-based Z-phase benefits from a denser distribution and a slower coarsening rate, and thus is recommended for alloy design.

Carbon is found to play the most critical role in the precipitation processes of Z-phase strengthened steels. An ultra-low C content and an optimal balance between Ta and N in a model alloy lead to the formation of a fine distribution of TaN in the as-tempered condition, which are transformed to blade-like Z-phase after short-term ageing. Such a low C content leads to very little formation of $M_{23}C_6$ at grain boundaries, which allows for the formation of a continuous film of Laves-phase there and a low impact toughness. Although, the addition of C results in precipitation of Ta(C, N), and hence a slower phase transformation to Z-phase, a low but not ultra-low carbon content is preferred in the new Z-phase strengthened steels.

Keywords: Creep, precipitation hardening, transmission electron microscopy, atom probe tomography, phase transformation, CrTaN, CrNbN, MX, M_2N, Laves-phase, coarsening, impact toughness.

Preface

The research work presented in this thesis was carried out in the Division of Materials Microstructure at the Department of Physics, Chalmers University of Technology, Gothenburg, Sweden, during the period May 2013 to December 2017, under supervision of Associate Professor Fang Liu and Professor Hans-Olof Andrén.

This project has been performed within the framework of the Swedish consortium for materials technology in thermal energy processes, KME (contract number: 510 and 710), the Swedish Energy Agency (contract number 31139-1), the Research Foundation of VGB (contract number: 348 and 397), and the Z-ultra project, which received funding from the European Union's Seventh Framework Program for research, technological development, and demonstration (grant agreement No. 309916).

List of appended papers:

Paper I

Core-shell structure of intermediate precipitates in a Nb-based Z-phase strengthened 12% Cr steel, Masoud Rashidi, Hans-Olof Andrén, Fang Liu, *Microscopy and Microanalysis, Vol. 23, 360-365, 2017.*

Paper II

A new 12% chromium steel strengthened by Z-phase precipitates, Fang Liu, Masoud Rashidi, Lennart Johansson, John Hald, Hans-Olof Andrén, *Scripta Materialia, Vol. 113, 93-96, 2016.*

Paper III

Coarsening rate of Z-phase precipitates in new Z-phase strengthened 12% Cr steels: experimental data and theoretical calculations, Masoud Rashidi, Joakim Odqvist, Lennart Johansson, John Hald, Hans-Olof Andrén, Fang Liu, *in manuscript*.

Paper IV

Microstructure and mechanical properties of two Z-phase strengthened 12% Cr martensitic steels: the effects of Cu and C, Masoud Rashidi, Lennart Johansson, Hans-Olof Andrén, Fang Liu, *Materials Science and Engineering A, Vol. 694, 57-65, 2017.*

Paper V

Transformation processes from precursor phases to Ta-containing Z-phase in 12% Cr Z-phase strengthened steels with varying C content, Masoud Rashidi, Ardeshir Golpayegani, Saad Sheikh, Sheng Guo, Hans-Olof Andrén, Fang Liu, *in manuscript.*

Paper VI

Tantalum and Niobium based Z-phase in a Z-phase strengthened 12% Cr steel, Masoud Rashidi, Robert Lawitzki, Hans-Olof Andrén, Fang Liu, *Proc. Eighth Int. Conf. Advances in Materials Technology for Fossil Power Plants, Eds J. Parker, J. Shingledecker and J. Siefert, ISBN 1-62708-131-3, ASM International, Materials Park OH, 2016, pp. 1060-1068.*

Paper VII

Microstructure of Z-phase strengthened martensitic steels: meeting the 650°C challenge, Fang Liu, Masoud Rashidi, John Hald, Lutz Reißig, and Hans-Olof Andrén, *Materials Science Forum, Vol. 879, 1147-1152, 2016.*

My contribution to the appended papers:

***Paper I*:** I performed the evaluation and interpretation of the results and wrote the paper under supervision of my advisors.

***Paper II*:** I performed the TEM experiments and co-authored the paper.

***Paper III*:** I performed the experiments and wrote the manuscript under supervision of my advisors.

***Paper IV*:** I performed SEM, TEM and APT experiments and wrote the paper under supervision of my advisors.

***Paper V*:** I performed SEM, TEM, and APT experiments and wrote the manuscript under supervision of my advisors.

***Paper VI*:** I performed SEM, TEM, and part of the APT experiments and wrote the paper under supervision of my advisors.

***Paper VII*:** I performed the experiments and co-authored the paper.

The following paper is also written during the period but due to the overlap with the above papers, it has not been included in the thesis.

Microstructure characterization of two Z-phase strengthened 12% chromium steels, Masoud Rashidi, Fang Liu, Hans-Olof Andrén, *in Proc. 10th Liège Conference: Materials for Advanced Power Engineering 2014, Eds. J. Lecomte-Beckers, O. Dedry, J. Oakey and B. Kuhn, pp. 71-80.*

In addition to the above papers, I contributed to the following papers, which are not included in the thesis:

Initial study of the microstructure of carbon fibres acting as negative electrodes in structural battery composites, Fang Liu, Masoud Rashidi, Leif Asp, *in Proc. 17th European Conference on Composite Materials, Munich, Germany, 2016.*

Graphitic microstructure and performance of carbon fibre Li-ion battery electrodes, G. Fredi, S. Jeschke, A. Boulaoued, J. Wallenstein, M. Rashidi, F. Liu, R. Harnden, D. Zenkert, J. Hagberg, G. Lindberg, P. Johansson, L. Stievano, L. Asp, *Submitted to Multifunctional Materials*

*Difficulties strengthen the mind, as **precipitates** do the **steel**!*

Inspired by Lucius Annaeus Seneca
Roman Philosopher

Table of Contents

List of Abbreviations

A-USC	Advanced Ultra Super Critical
APT	Atom Probe Tomography
bcc	Body Centered Cubic
bct	Body Centered Tetragonal
BSE	Backscattered Electron
CBED	Convergent Beam Electron Diffraction
EDXS	Energy Dispersive X-ray Spectroscopy
fcc	Face-Centered Cubic
FEG	Field Emission Gun
HAADF	High Angle Annular Dark Field
HCP	Hexagonal Close-Packed
M_f	Martensitic finish temperature
M_s	Martensitic start temperature
PAGB	Prior Austenite Grain Boundary
SE	Secondary Electron
SEM	Scanning Electron Microscopy
TEM	Transmission Electron Microscopy
XRD	X-ray Diffraction

List of Figures

Chapter 1

Introduction

A true conservationist is a man who knows that the world is not given by his fathers, but borrowed from his children.

John James Audubon
An American naturalist (1785-1851)

1.1 Energy security and environmental protection

Energy security and environmental protection are regarded as extremely essential issues throughout the world and much attention is paid to the climate change and limiting CO_2 emissions. Renewable energy sources such as wind and solar energies, which do not emit CO_2 have been increasing remarkably. However, the total share of electricity production from wind and solar is still rather small on a worldwide scale, and it seems unlikely that the production will increase so quickly that other energy sources such as fossil-fuel power plants will be terminated for the foreseeable future. Thus fossil-fired power plants will remain as important weather-independent basic energy suppliers[1]. Fossil-fired power plants account for about one third of the global CO_2 emissions [2]. Considering the fact that these power plants will run for decades, it is important to limit their fuel consumption and CO_2 emissions via enhancing the energy conversion efficiency in new steam power plants, mainly through increasing the operating steam temperature and pressure. However, the efficiency is often limited by the availability of economically viable structural

materials with good long-term corrosion and creep resistance against the increased temperature and pressure. Martensitic 9–12% Cr steels offer an optimal combination of the critical properties, i.e. creep strength, corrosion resistance, thermal conductivity and thermal expansion, at a relatively low cost [3] and are used in the critical components of such power plants. The development of ultra supercritical power plants started in the 1980s. Since then progressive increase in steam temperature and pressure has been achieved, and now power plants with steam temperatures up to 620°C have been successfully built [4, 5]. The net efficiency of subcritical power plants (167 bar and 538°C) is below 38%, and it reaches almost 45% in ultra-supercritical power plants (285 bar and 620°C) [6].It was estimated that for a typical 700 MW power plant, a gain in the net efficiency by 1 percent unit can reduce emissions by 2.5 million tonnes CO_2, 2000 tonnes NO_X, and 2000 tonnes SO_2 over a 30-year life time [7].

By considering the increasing share of renewable energies in many countries, there is a great demand on the flexibility of thermal power plants, in order to compensate for the fluctuating input from solar and wind energy [8, 9]. Martensitic/ferritic steels are better suited for this application, since they have higher thermal conductivity (provides faster heat transfer rates when the temperature of the component changes) and lower thermal expansion coefficient (provides more structural stability) compared to austenitic steels and Ni-base alloys [5, 10]. In connection to flexible operations of power plants, a stronger material provides the possibility of reducing the thickness of the components, and hence reducing thermal stresses during frequent start-up and shut-down cycles. Besides, ferritic steels contain lower amounts of expensive elements and are thus cheaper compared to the austenitic ones [11, 12].

1.2 Motivations for alloy development

Tempered martensitic/ferritic 9–12% Cr steels have been successfully used in critical components of fossil-fired steam power plants. These steels are used in the power plants for thick-section critical components such as main steam pipes, headers, and large forgings [3, 13], 14]. This family of steels is also used for production of large castings for turbine casings and steam valve bodies [7].

Water is used as the working fluid in thermal power plants, see **Figure 1.1**. A boiler is used to produce hot steam. The high pressure and high temperature steam then rotates the blades of a turbine and thus produces electricity through a generator. A higher steam temperature and pressure leads to a higher thermal efficiency in the power plants.

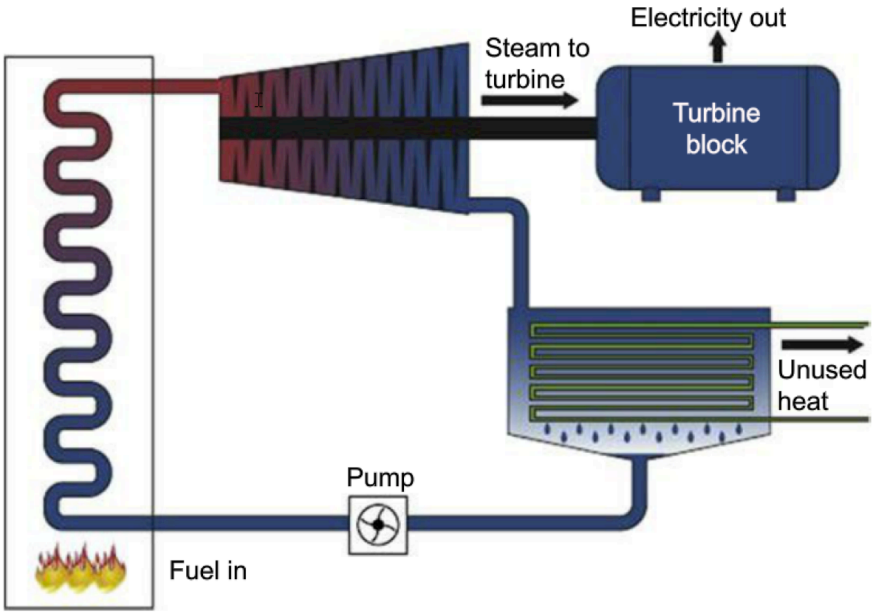

Figure 1.1 Schematic drawing of a fossil-fired steam power plant with water as the working fluid [6].

According to the Carnot cycle, the efficiency of steam power plants is affected by the steam temperature. The efficiency η can be calculated according to:

$$\eta = 1 - \frac{T_C}{T_H} \qquad \textbf{Equation 1-1}$$

where T_C is the absolute temperature of the condensed water and T_H is the absolute temperature of the steam. However, the Carnot cycle cannot be reached practically. It is worth mentioning that in practice, the Rankine cycle with reheating is used in steam power plants. Super critical power plants are operated above the critical point of water, i.e. 374°C and 220 bar. **Figure 1.2** summarises the operational parameters for the fossil-fired power plants.

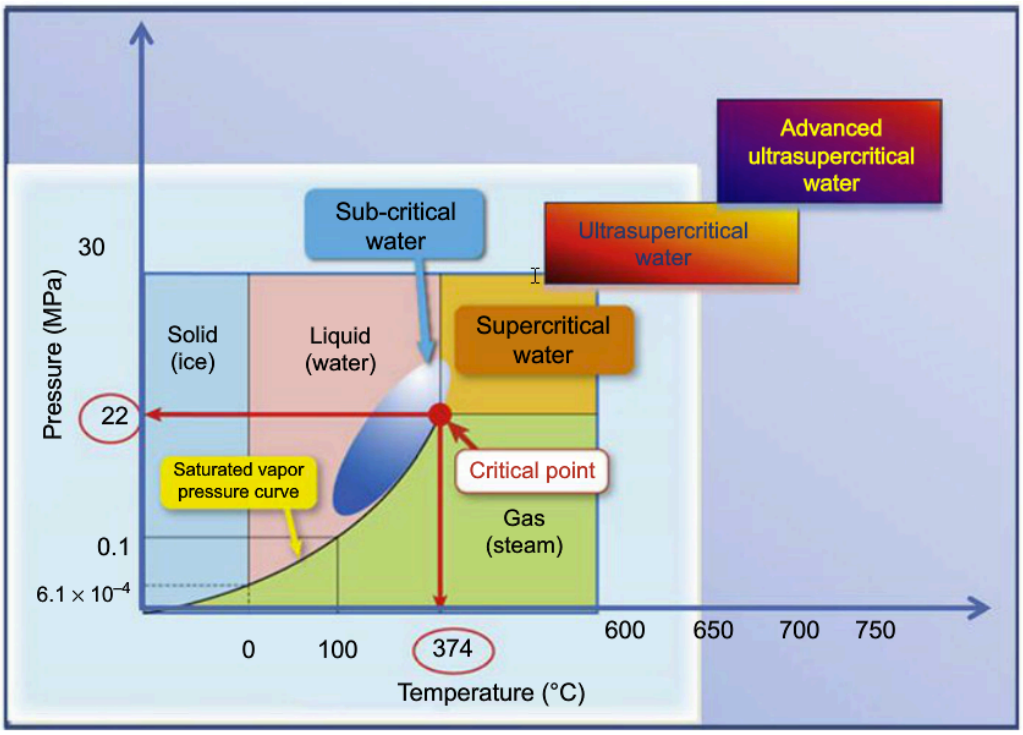

Figure 1.2 Water equilibrium diagram and the operational parameters of thermal power plants [6].

Considering the fact that fossil-fired steam power plants produce more than 60% of the world's electricity [2], there is always an interest in increasing the thermal efficiency of these power plants, in order to minimize the fuel consumption and CO_2 emissions. Developing creep resistant steels that can be used at higher steam temperatures and pressures for longer times is the prerequisite to increase thermal efficiency. The extreme conditions of high steam temperatures and steam pressure will worsen the classic problems for high-temperature materials, such as creep, and oxidation. Low chromium steels and 9% Cr steels, which have been used to a large extent for steam power plants, do not provide proper creep and corrosion resistance for the higher steam temperature of 650°C. Thus, there is a need for better materials to withstand such extreme conditions.

1.3 Scope of this work

This research was undertaken in order to evaluate the feasibility of using precipitates of a thermodynamically stable phase, Z-phase, as strengthening agent to achieve proper creep strength at a steam temperature of 650°C. Moreover, the role of other precipitates on the mechanical properties of Z-phase strengthened steels was also studied.

The work was done in a close collaboration between Chalmers University of Technology, Technical University of Denmark, Siemens Industrial Turbomachinery AB, and the partners of the Z-Ultra consortium: Saarschmiede GmbH, Fraunhofer Institute for Mechanics of Materials, RWE power AG, Paton Electric Welding Institute, Technical University of Graz, Engineering Academy of Armenia, Georgian Technical University, IPP Centre LLC, the Institute of Physics of Materials of the Academy of Sciences of the Czech Republic.

Chapter 2

Background

Men are like steel. If they lose their temper, they lose their strength.

Inspired by Chuck Norris
An American Artist

2.1 Iron and steel

Iron has a body-centered cubic (bcc) structure (α-iron or ferrite) at room temperature and this structure is stable up to 910°C. In the temperature range of 910°C to 1390°C, iron has a face-centered cubic (fcc) structure, which is called γ-iron or austenite. Above 1390°C, iron returns to bcc structure and forms δ-ferrite, which is stable up to the melting temperature of 1536°C, see **Figure 2.1**. These changes in structure are very important and affect the physical and mechanical properties of the material.

Iron alloys with less than 2 wt.% C are generally classified as steel. Low carbon steels contain up to 0.3 wt.% C. Medium carbon steels contain 0.3 to 0.8 wt.% C and steels with higher carbon content are classified as high carbon steels. Steels are often the "gold standard" against other structural materials. Thanks to the regular and exciting discoveries in the context of iron and its alloys, steels remain as the most successful and cost-effective of all materials. Steels help improving the quality of our everyday life with the consumption of more than a billion tones per year [15]. One reason for such a high consumption of steels is the endless variety of properties and

microstructure that can be achieved by altering composition and processing parameters.

Among all different grades of steels, creep resistant 9–12% Cr steels, the alloys of interest in this thesis, have been successfully used in different parts of fossil-fired steam power plants.

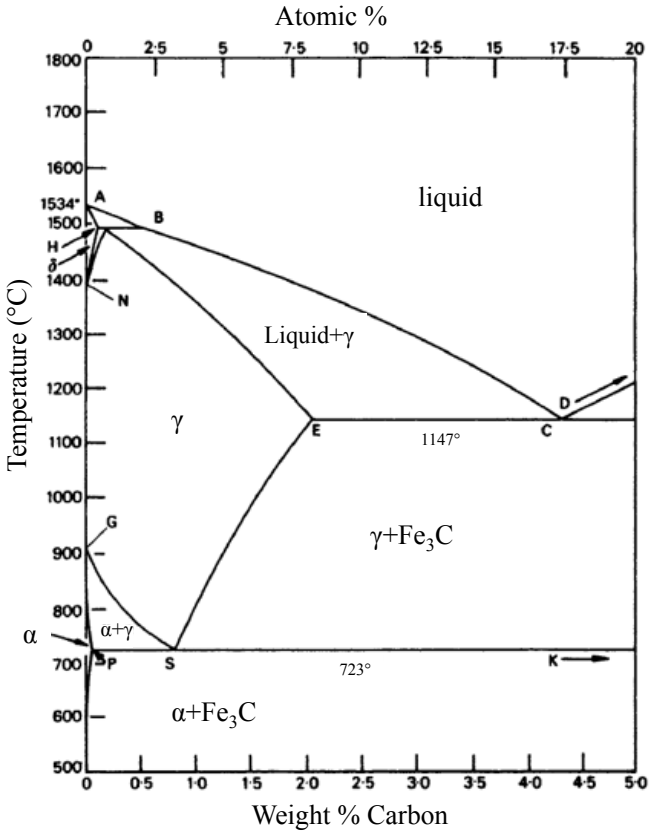

Figure 2.1 The metastable (Fe_3C containing) iron-carbon phase diagram [16].

2.2. Creep

Creep is a slow and continuous plastic deformation of materials under mechanical stress for a prolonged period of time. Creep can occur at any temperatures above zero Kelvin, however it is traditionally associated with time-dependent plastic deformation of a material at elevated temperatures often higher than $0.4T_m$ (T_m is absolute melting temperature of the material) under a mechanical stress below the yield stress of the material [17, 18].

For steels, creep tests are mostly done at a constant load and temperature. The obtained results from tests are presented as creep curves, which graphically represent the time-dependence of strain. In **Figure 2.2**, three stages of creep, primary or transient creep, secondary or steady-state creep, and tertiary or accelerated creep, are schematically shown [18].

The instantaneous strain, ε_0 is a combination of elastic strain and possible plastic strain depending on the tensile stress level. In the region between ε_0 and ε_1, primary creep region, creep rate decreases with time due to strain hardening or a decrease in free or mobile dislocations. Between ε_1 and ε_2, the creep rate remains constant and a steady-state creep rate is achieved mainly due to a balance between generation and recovery of dislocations. In the tertiary creep stage, the creep rate increases with time until rupture. Necking of the specimen and formation of cavities reduce the cross-section and thus increase the stress under constant load. The increase in the creep rate in tertiary stage can also be attributed to the microstructure evolution during creep. This evolution usually consists of dynamic recovery, dynamic recrystallization, and coarsening of precipitates [18]. In **Figure 2.2**, the idealized creep and creep rate curves are shown. However, creep-resistant steels mostly exhibit a different creep behavior. The steady-state stage is absent and after the transient creep stage, the accelerated creep starts and thus a minimum creep rate is introduced instead of the steady-state creep stage [18]. Microstructural evolution such as phase transformations, dissolution or coarsening of precipitates after an extended period can also result in a more complicated behavior during creep. The creep rupture data are usually presented in a graph showing the relationship between σ, applied stress, and t_r, time to rupture.

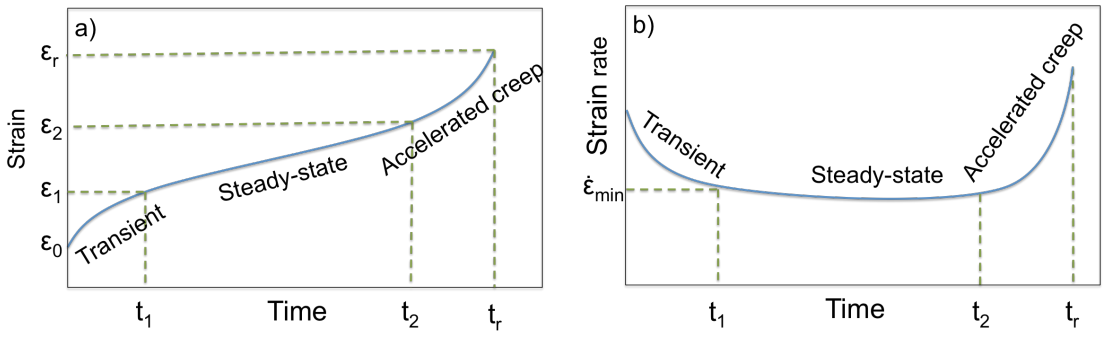

Figure 2.2 Schematic drawing of a) creep curve and b) creep rate curve under constant tensile load and constant temperature.

Ashby [19] proposed a deformation mechanism map, which displays the dominant deformation mechanism depending on the stress and temperature of deformation. The deformation mechanism maps can provide a qualitative way to select materials for engineering application and/or predict the mechanism by which the material is deformed. Based on Ashby's deformation mechanism map, at technically interesting stress levels and temperatures, dislocation creep is the dominant mechanism for creep of 9–12% Cr steels i.e. creep occurs mainly via climb and glide of dislocations in the lattice, and the principles to achieve creep resistance is to obstruct the dislocation movement [20, 21].

2.3 9–12% Cr steels

The 9–12% chromium steels with tempered martensitic structure combine sufficient corrosion and creep resistance at a relatively low cost for critical components in the fossil-fired thermal power plants. The common alloying elements used in 9–12% Cr steels are: Ni, Mn, Co, Si, Mo, Cu, W, Nb, V, Ta, N, and B [23].

2.3.1 Physical metallurgy

The alloying elements in 9–12% Cr steels affect the stability range of austenite and ferrite in this family of steels, which is very important to achieve a tempered martensitic structure.

Austenite stabilizing elements increase the stability range of austenite by dropping A_3 temperature (below A_3 temperature, austenite to ferrite transformation becomes thermodynamically possible) and increasing A_4 temperature (above A_4 temperature, austenite to δ-ferrite transformation becomes thermodynamically possible). Elements like C, N, Mn, Ni, Cu, and Co are austenite stabilizers in iron. On the other hand, the ferrite stabilizer elements such as Si, Mo, W, V, Nb, and Ti decrease the austenite stability region by raising A_3 temperature and dropping A_4 temperature [22, 23].

By cooling down the steel from the austenite region, phase transformation can occur. This phase transformation can be a diffusion-based transformation (ferrite and pearlite) or a shear process with no diffusion (martensite). Any increase in the concentration of ferrite stabilizer elements promotes formation of δ-ferrite that is detrimental to the toughness of these alloys and decreases the creep strength [24]. Depending on the alloying elements, 9–12% Cr steels may contain some small amount of δ-ferrite [25].

Carbon, and many other alloying elements have different solubility in different phases of iron and this is the basis for heat treatment of steel. Heat treatment controls the microstructure through heating and cooling cycles and results in different mechanical properties for different applications. The typical heat treatment for 9–12% Cr steels is an austenitization heat treatment, which is followed by quenching and a tempering treatment [23].

During austenitization, within the austenitic region (see **Figure 2.1**), the steel is heated up above A_3, the ferrite/austenite transformation temperature. Primary carbides and nitrides are dissolved in the matrix. This is required for later precipitation of fine secondary carbides/nitrides. Austenitization is normally done at temperatures in the range between 1020°C and 1150°C. At a low austenitization temperature, some primary particle might not dissolve during the heat treatment, which results in less solid solution of alloying elements for precipitation of secondary precipitates. However, some undissolved primary particles are beneficial to restrict the grain

growth. During austenitization, these undissolved particles pin the austenite grain boundaries and control the grain growth [26]. At higher austenitization temperature, the concentration of solute elements in the matrix increases. This will result in an increased volume fraction of secondary precipitates.

When a steel is quenched (i.e. cooled rapidly enough that no diffusional transformation occurs during cooling) from the austenitic range to room temperature, a brittle and hard phase, martensite, is formed. Martensite is the resulting structure of this diffusionless transformation, and is a super-saturated solid solution of carbon and possibly nitrogen in iron. Martensite has a body centered tetragonal (bct) structure and the c/a ratio varies with C content. The crystal structure of martensite is relatively closer to the ferrite than the austenite; therefore martensite is generally designated as α′. During the martensitic transformation, no diffusion of C occurs and thus the composition of martensite is the same as austenite. In a steel with a specific composition the martensitic reaction occurs within a specific temperature range, between martensitic start temperature (M_s), and martensitic finish temperature (M_f). The ability of a steel to form martensite during cooling or quenching depends on its hardenability. 9–12% Cr steels develop good hardenability and thus even in 12% Cr rotors more than one meter in diameter, martensitic transformation occurs both in the center and at the surface of the forging [27]. The M_s temperature for 9–12% Cr steels is around 400°C and M_f is around 200°C [28].

As a result of martensitic transformation in 9–12% Cr steels, lath martensite forms. Lath martensite consists of thin plates growing in one direction and parallel to each other. These parallel plates are separated by low angle boundaries. The width of the laths within a packet is in the range of a few hundred nanometers. The martensite contains a high density of dislocations [13].

Martensite is a brittle phase and it is essential to apply further heat treatment, tempering, before putting the steel into service. Therefore the tempering treatment is done after austenitization and quenching. During tempering, martensite is heated up below A_1, the ferrite/austenite transformation temperature, and carbides and nitrides are formed by a diffusion-controlled transformation. The result is a fine distribution of carbides and/or nitrides in a ferritic matrix, which is the basic structure for the family of 9–12% Cr steels [25].

Tempering of 9–12% Cr steels aims to form secondary precipitates from the super saturated solid solution, reduce internal stresses and recover the dislocation structure. **Figure 2.3** shows schematically the microstructure in 9–12% Cr steels after tempering. Some of the dislocations are recovered during tempering. Depending on the composition of the steel, Laves-phase and/or $M_{23}C_6$ particles precipitate on the boundaries and MX precipitates on the boundaries as well as inside the laths. Tempering temperature in 9–12% Cr steels is done either in the range of 650–720°C

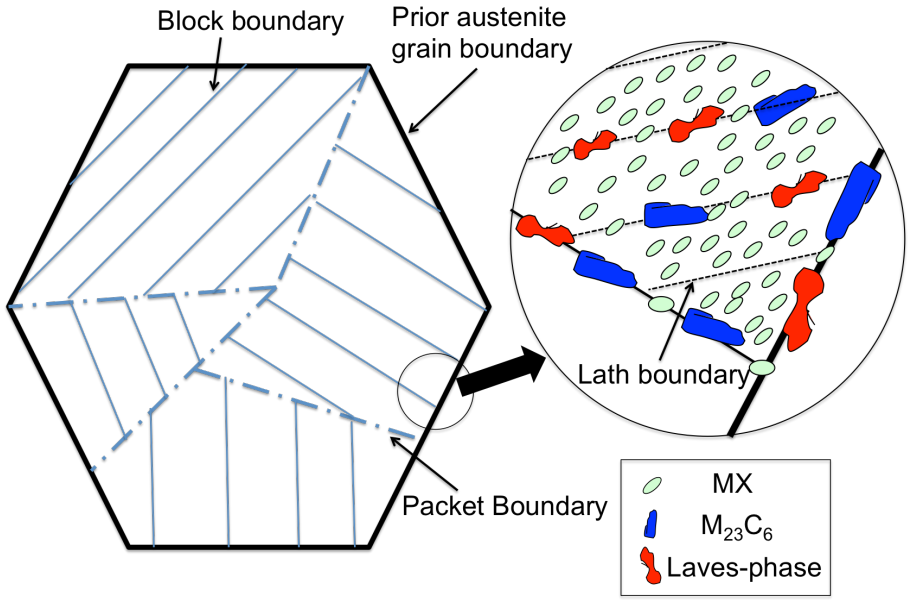

Figure 2.3 Schematic illustration of the boundaries and the precipitates of the tempered martensite in 9–12% Cr steels.

for big components, where high tensile strength is important or in the range of 730–780°C for small components, where toughness is important [29].

2.3.2 Strengthening mechanisms

The strengthening mechanisms in creep-resistant steels with an emphasis on tempered martensitic 9–12% Cr steels are briefly described in this section. The four strengthening mechanisms for creep-resistant steels are solid solution hardening, precipitation hardening, dislocation hardening, and boundary hardening. Even though in this family of steels, a combination of strengthening mechanisms provides the creep strength at elevated temperatures, precipitation hardening is regarded as the most important mechanism.

Solid solution hardening

Based on the Hume-Rothery rules (atomic size factor, electrochemical effect, and relative valence effect), substitutional atoms such as Mo and W are effective solid solution strengthener in 9–12% Cr steels. These elements have much larger atomic size compared to that of the solvent iron and are considered as effective solid solution strengthener in this family of steels [29]. The beneficial effect of these elements to hinder dislocation climb and glide can only be maintained if they remain in the solid solution. However, the addition of these elements to the steels results in precipitation of $Fe_2(W, Mo)$, Laves-phase, during tempering/service [30, 31], and hence the contribution of these elements to the solid solution hardening is decreased.

Precipitation hardening

Precipitation hardening is one of the important strengthening mechanisms in creep-resistant steels and especially in 9–12% Cr steels at elevated temperatures. Precipitates such as $M_{23}C_6$, MX, and M_2X (M stands for the metallic element, and X is carbon and/or nitrogen), intermetallic compounds such as Fe_2(Mo, W) Laves-phase, and metallic phases, such as Cu, can contribute to the strength of the 9–12% Cr steels. A fine distribution of precipitates within the matrix and at the boundaries enhances the dislocation hardening and boundary hardening by stabilizing the free dislocations in the matrix and sub-grain structure [32].

Several mechanisms have been proposed to calculate the stress needed for a dislocation to pass a particle. These mechanisms are Orowan mechanism, local and general climb mechanism, and Srolovitz mechanism, which are explained in detail in reference [29].

According to the Orowan mechanism, the stress (σ_{or}) required for a dislocation to pass a particle is calculated through the following equation [29]:

$$\sigma_{or} = 0.8 \frac{MGb}{\lambda} \qquad \textbf{Equation 2-1}$$

Where M is Taylor factor (=3), G is the shear modulus, b is the Burgers vector, and λ is the average interparticle distance. The interparticle distance is related to the volume fraction and the mean size of the particles. The climb mobility of dislocations increases with increasing temperature, which reduces the precipitation hardening effect. Using the Orowan equation thus overestimates the precipitation hardening effect, as only part of the dislocations would bow around the precipitates. Magnusson and Sandström [20, 33] provided a detail description of the climb mechanism and the effective Orowan stress for 9–12% Cr steels.

In 9–12% Cr steels, λ increases by coarsening of $M_{23}C_6$, Laves-phase, and MX, or dissolution of MX to form massive Z-phase precipitates. Increasing the λ results in weakening the material over long periods of time. Coarsening or dissolution of fine particles near grain boundaries results in localized weak zones and promotes premature creep rupture due to localized creep deformation. The technically interesting stress and temperature ranges for 9–12% Cr steels during service exposure and creep testing are 20 MPa to 250 MPa and 500 °C to 700 °C. In these ranges, dislocation creep is the main creep mechanism, which leads to glide and climb of free dislocations and movement of sub-boundaries. Precipitation hardening is mainly employed to delay the deformation process by pinning dislocations and sub-boundaries [13, 34, 35].

Dislocation hardening

Once a dislocation acts as an obstacle for a moving dislocation, dislocation hardening occurs [5]. As a result of martensitic transformation in 9–12% Cr steels, a high density of dislocations is produced, which provide dislocation hardening as an important strengthening mechanism at room temperature. However, at elevated temperature, these excess dislocations accelerate recovery and recrystallization of deformed microstructure during creep. The dislocation density in this family of steels can be controlled via tempering treatment. In the as-tempered condition and depending on the tempering temperature, the dislocation density varies in the range of $1–10 \times 10^{14}$ m^{-2} in the matrix. In 9–12% Cr steels, normally a lower tempering temperature gives a better creep resistance for shorter times below 15,000 h and a high tempering temperature gives better creep results for long-term creep tests. This behavior is mainly attributed to the presence of excess dislocations after low temperature tempering which can accelerate the recovery and recrystallization for longer creep test time [29].

Sub-boundary hardening

After austenitization and tempering, 9–12% Cr steels show a lath martensitic microstructure consisting of a high density of dislocations and a dispersion of precipitates in the matrix and along the boundaries. These boundaries provide the sub-boundary hardening, which is given by [29]:

$$\sigma_{\mathrm{sb}} = 10\frac{\mathrm{Gb}}{\lambda_{sg}} \qquad \textbf{Equation 2-2}$$

Where λ_{sg} is the short width of the elongated lath boundaries in the range of a few hundred nm in the tempered martensitic 9–12% Cr steels. The usually obtained values [29] for sub-boundary hardening in 9–12% Cr steels show the contribution obtained from sub-boundary hardening is much greater compared to the values obtained from Orowan stress for $M_{23}C_6$, MX, and Laves-phase particles. Therefore, sub-boundary hardening gives an important contribution to the creep strength of the tempered martensitic 9–12% Cr steels.

The mobile nature of lath and block boundaries mainly in the accelerated creep region results in increasing the λ_{sg}. The movement of these boundaries absorbs the excess dislocations and results in softening through a dynamic recovery process. The fine distribution of $M_{23}C_6$ and MX precipitates along the boundaries stabilizes the boundaries and provides a pinning force against the movement of boundaries and thus retards the increase in the λ_{sg} during creep. Thus, particle-stabilized substructure hardening is the most important mechanism in 9–12% Cr steels to obtain long-term creep resistance [13, 36].

In short, the contribution from solid solution hardening of W and Mo decreases to a great extent after precipitation of Laves-phase precipitates during creep. The strengthening effect from dislocation hardening also cannot maintain a long-term creep resistance. The contribution from sub-boundary hardening can also disappear due to the mobile nature of boundaries at high temperatures. Thus precipitation hardening and particle-stabilized sub-boundary hardening are regarded as the main strengthening mechanisms for creep-resistant 9–12% Cr steels.

2.3.3 Precipitates in 9–12% Cr steels

In 9–12% Cr steels, the precipitation processes occur during tempering treatment as well as during service/ageing. The precipitation process is typically divided into three stages: nucleation, growth and coarsening.

The nucleation process of precipitates is very important for the creep strength. If a precipitate has a high nucleation rate, a fine distribution of precipitates is obtained, which improves the mechanical properties. On the other hand if a precipitate has a low nucleation rate, once some precipitates nucleate, and they have enough time during growth to consume the necessary elements in their vicinity to prevent further nucleation there. Thus a low density of precipitates with large sizes is formed, which do not provide optimal precipitation hardening. The nucleation rate is controlled by the availability of the necessary elements in the matrix, thermodynamic driving force, and interfacial energy. Nucleation of precipitates is mostly heterogonous. Non-equilibrium defects such as dislocations, grain boundaries, and inclusions are some of the possible nucleation sites for precipitates [37].

When a nucleus has reached a certain critical size, it grows. During the growth process, the sizes of the precipitates increase until the equilibrium volume fraction is reached. The growth rate is controlled by diffusion and the availability of necessary elements in the matrix/precipitate interface [37].

Coarsening of precipitates is a result of dissolution of small precipitates and growth of bigger ones while the volume fraction of precipitates remains constant. The coarsening behavior of precipitates is very important for long-term creep strength. Once coarsening process starts, a high number density of small precipitates gradually transforms to a lower number density of big precipitates. The driving force for coarsening is to decrease the total interfacial energy since a few bigger particles have less surface area compared to many small precipitates. Generally a fine distribution of precipitates gives higher strength. Therefore, coarsening of precipitates results in a loss in strength [37].

The coherency of the particle with the matrix plays an important role in the coarsening behavior of the precipitate especially if the precipitate and the matrix have different crystal structures; coherent and semicoherent interfaces have a low

interfacial energy and therefore coarsen very slowly while incoherent interfaces have a high interfacial energy and thus coarsen faster [37].

In tempered martensitic 9–12% Cr steels a wide variety of precipitates may form depending on the composition of the steel and thermal history. The most important precipitates in this family of alloys are the following:

Metastable precipitates

In 9–12% Cr, depending on the composition of the steel and the temperature of service, there are both metastable and stable precipitates. Some of the precipitates have very short lifetime and are already dissolved during tempering treatment. M_3C and M_7C_3 are typical metastable precipitates that are already dissolved and replaced by a thermodynamically more stable phase, $M_{23}C_6$, during tempering treatment [38]. The presence of M_7C_3 and M_3C also depends on the content of MX forming elements such as V and Nb [39].

$M_{23}C_6$

$M_{23}C_6$ precipitates mostly on the boundaries in 9–12% Cr steels and dissolves all metastable carbides (except MX) during tempering treatment. It has a cubic crystal structure, consists of mainly Cr and C and minor amounts of Fe, Mo, W, and B. The size of $M_{23}C_6$ in the as-tempered condition is approximately 80–100 nm in 9–12% Cr steels [40]. $M_{23}C_6$ precipitates enhance the sub-boundary hardening as well as precipitation hardening, i.e. Orowan stress. In traditional 9–12% Cr steels without B addition, $M_{23}C_6$ precipitates coarsen quickly during creep. Thus it was suggested to limit the C content to 0.02 wt.% to enhance the formation of MX precipitates instead of $M_{23}C_6$. However, recent investigations have shown that the addition of B significantly decreases the rate of Ostwald ripening of $M_{23}(C, B)_6$, and thus the fine distribution of $M_{23}(C,B)_6$ can be maintained in the vicinity of PAGBs during exposure at high temperatures [41– 43].

Laves-phase

The addition of W and/or Mo results in the precipitation of Laves-phase, $Fe_2(W, Mo)$. This intermetallic phase also contains Cr and Si [44, 45] and has a hexagonal crystal structure. The Laves-phase formation results in depletion of W and Mo from the matrix and subsequently a decrease in the solid solution hardening obtained by Mo and W in the matrix. However, formation of a fine distribution of Laves-phase can provide precipitation hardening. Thus Laves-phase distribution must be controlled in order to improve the creep resistance [46– 48]. W-containing Laves-phase usually nucleates faster and hence a finer distribution of Laves-phase may be achieved compared to the Mo-based Laves-phase.

MX

MX precipitates (M= V, Nb, or Ta and X = C and/or N) are coherent and semicoherent precipitates, which provide precipitation hardening to the 9–12% Cr steels. MX precipitates are located inside the matrix and at the PAGBs, packet, block, and lath boundaries [49]. The coarsening rate of MX precipitates is slow in 9–12% Cr steels and thus they are useful for long-term creep strength [42, 50]. In most 9–12% Cr steels containing Nb and V, MX precipitates can be divided in two groups of NbC and VN. Spherical NbC precipitates remain undissolved after austenitization treatment and are thus called primary MX particles. The VN precipitates are formed during tempering and are hence named secondary precipitates. Both primary and secondary MX precipitates have a low coarsening rate. Secondary MX precipitates are known for their fine distribution and contribution to the creep resistance of the steels [40].

M_2X

The M_2X precipitate with a hexagonal crystal structure is generally of type Cr_2N in 9–12% Cr steels. Part of Cr can be replaced with V, Nb, and Ta [51]. Sawada reported that in 9% Cr steels, a low tempering temperature (680°C) results in the formation of M_2X as well as MX and $M_{23}C_6$, while no M_2X could be seen in the same steels after tempering at a higher temperature (765°C) [52]. Agamennone reported that the formation of M_2X as a result of a low temperature tempering (570°C) promoted the formation of Z-phase in a 12% Cr steel compared to the high temperature tempering (760°C), where no M_2X was observed [53]. The precipitation sequence of M_2X, MX, and Z-phase during creep is not clear. The contents of Cr, C, N, and MX forming elements of V, Nb, and Ta as well as the tempering temperature are important parameters affecting the stability of these phases in the 9–12% Cr steels.

Z-phase

Z-phase (CrMN, M=V, Nb, Ta) is the most stable nitride in 9–12% Cr steels at the temperature range of approximately 550–700°C [54].

The original Z-phase, CrNbN, was first seen in 1950 in Nb alloyed creep-resistant austenitic steels [55]. A fine distribution of rod-like precipitates resulted in precipitate hardening in these alloys [56]. The crystal structure of Z-phase was first characterized in 1972 as tetragonal in austenitic steels [57].

In 1985, Karlsson et al. [58] observed particles with Z-phase composition but with an fcc crystal structure in austenitic steels after ageing at 750°C. Half of the Nb in these particles were replaced by V and they were thought to be a precursor phase to Z-phase. Danielsen et al. reported that the cubic structure coexists with the tetragonal structure in Z-phase precipitates [59]. Further investigation showed that tetragonal structure is predominant after long-term exposures while cubic structure was found in short-term exposed specimens [60].

In 1986, Schnabel et al. [61] observed a V containing Z-phase in a martensitic 11Cr-1Mo-VNbN steel which showed a dramatic loss in creep and for the first time, Strang and Vodarek [62] drew the connection between large Z-phase precipitates and the loss of creep strength. They found that Z-phase grows at the expense of small beneficial MX precipitates. The crystal structure of this V containing Z-phase had smaller lattice parameters compared to the original one and thus Cr(V,Nb)N was named as modified Z-phase [35]. This modified Z-phase precipitates after long-term exposure and only few coarse precipitates are formed.

The Cr content has a strong influence on precipitation of Z-phase and the precipitation is much faster in 11-12% Cr steels compared to 9% Cr steels [54, 63].

2.3.4 Historical development

The development of 9–12% Cr steel is achieved by small but important changes in the composition of the steels, especially in elements such as N, V, Nb, B, and W. The addition of these alloying elements controls the behavior of the precipitates they form in the as-tempered condition and/or during service.

Up to the 1920s, carbon steels were generally used for components in steam power plants. These steels were exposed to a maximum temperature of 350°C at a pressure of 15 bar. Low-alloyed steels were introduced in the beginning of the 1920s and thus the operating temperature in the power plants was increased to 450°C with a pressure of 35 bar. Until the 1950s, some alloying elements such as Mo, Mn, Si, Cr, and V were added to the steels to improve their high temperature strength and corrosion resistance [25].

The first leap for developing 9–12% Cr steels was in the 1950s, when the development of thermal power plants operating at a steam temperature of 538°C–566°C for power supply began. The second leap was in the 1980s when the goal was to develop low-pollution power plants operating at higher steam temperatures of 600°C–650°C and supercritical pressures up to 350 bar. Since the 1980s, many national and international research projects have been in progress in Japan, USA, and Europe [25].

Some of the important factors resulting in the development of creep resistant steels are: long-term operational experience and creep tests, improvements in melting technology, understanding of the microstructure evolution of the steels during long-term creep testing, systematic investigation on the effect of different alloying elements and using computer aided alloy design, development of methods and equipment to identify precipitates (e.g. TEM), etc [25].

Achievements

X22CrMoV, containing 12% Cr and 1% Mo, is one of the early tempered martensite ferritic steels that was developed in Germany in the 1950s. Its creep strength is based on solid solution hardening and precipitation of $M_{23}C_6$ carbides [25].

Adding Nb and N into steels, for example H64 (UK), FV448 (UK), and 56TS (France), resulted in further increase in strength by precipitation of secondary MX precipitates of type VN and Nb(C, N). Boron was recognized as a beneficial element for improving creep strength by stabilizing $M_{23}(C, B)_6$ [64, 65], for example in the TAF steel (Japan).

The steel 9Cr1MoV or the so-called P91 steel was developed in USA in the late 1970s originally to manufacture pipes and vessels for fast breeder reactors. At present, it is widely used in fossil-fired steam power plants in pressure vessel and piping systems. P91 is tough, weldable and has a creep strength of 94 MPa at 600°C for 100,000 h [11, 25]. The microstructure of this steel in the as-tempered condition consists of a lath martensite, which is stabilized by $M_{23}C_6$ carbides and MX carbonitrides [28].

In Europe, under the COST program, the pipe steel E911 was developed. This alloy contains 9% Cr and its creep rupture strength is 98 MPa at 600°C for 100,000 hours [25, 50]. NF616 (also called P92) is a 9% Cr pipe steel, alloyed with C, Mo, W, V, Nb, N, and B that was developed in the second half of the 1980s in Japan. Its creep rupture strength is 113 MPa at 600°C for 100,000h [25, 50].

MARBN, a martensitic steel strengthened by boron and MX nitrides is designed based on stabilization of martensitic microstructure in the vicinity of PAGBs, is a candidate material for critical components in advanced ultra supercritical power plants (A-USC) in Japan [66]. A low-carbon 9Cr steel (based on lower Ni and Al) [5], SAVE12 (a 12% Cr steel, high B and low N) and SAVE12AD (lower Cr content of 9% to achieve long-term stability of martensite) are other candidate materials to be used in A-USC power plants [5].

In Europe, the development of 9–12% Cr steels resulted in demonstration of a large rotor forging with the highest potential for 620°C application, which is a 9Cr steel, FB2. There is an attempt to further optimize the composition of MARBN for 650°C application [67].

A new martensitic steel, G115, was developed in the period of 2006 to 2015 in China. This steel is introduced as a candidate material for manufacturing of large scale pipes, valves, and forgings for the temperatures up to 630°C. G115 contains only 9% Cr to balance the corrosion properties and creep resistance. The addition of 3% Co and 3% W are introduced as main improvements compared to P92 [68– 70].

Failures

There are several mechanisms responsible for the degradation in creep strength at long times: precipitation of a more thermodynamically stable phase at the expense of the fine family of carbonitrides, preferential recovery of martensite at the PAGBs, coarsening of laths and precipitates, recovery of excess dislocations as a result of low temperature tempering, adverse effect of δ-ferrite and loss of creep ductility. It is possible that a combination of several mechanisms lead to a creep loss, however, it is difficult to quantify the contribution of each mechanism to the failure. Thus, in most of the cases, a dominant mechanism is introduced as the degradation mechanism for loss of creep resistance. To develop creep resistant steels for 650°C steam applications, it is also necessary to consider the oxidation resistance of the steels [5]. The oxidation resistance improves with increasing Cr content and in terms of oxidation, at 650°C, 12% Cr steels are superior to 9% Cr steels [71– 73]. Within the European COST program, a number of alloys were tested at 650°C for rotor applications. These alloys contained 10-11% Cr and varying amount of V, Nb, N, B, Mo, Mn, Si, and C. The trial steels showed good creep strength for short-term creep tests below 10,000 h. However in the period between 10,000-20,000 h, a reduction in creep rupture strength was seen. Based on the results of microstructure characterization of these trial steels, the dominant degradation mechanism in loss of creep resistance is attributed to a phase transformation from small MX to coarse Z-phase precipitates [74]. The nucleation of Z-phase is a slow process [75], and thus once a Z-phase precipitate is formed, it starts to consume the neighbouring small MX particles and thus becomes a huge Z-phase precipitate, which does not contribute to the creep strength of the material [35, 76].

Investigation of a number of 9–12 % Cr alloys revealed that in low Cr content alloys (8–9%), even after very long time, very few Z-phase was formed and a fine distribution of MX was preserved. However, for a Cr content above 10.5 wt.%, Z-phase precipitation occurred extensively, resulting in a reduction of creep strength [13, 49].

2.4 Z-phase strengthened steels

To increase the steam temperature in thermal power plants up to 650°C, it is necessary to use 11–12% Cr steels to ensure a sufficient oxidation resistance. However, it was found that in the 11–12% Cr ferritic martensitic steels that are strengthened by (V, Nb)N particles, precipitation of the thermodynamically stable Z-phase, Cr(V,Nb)N, is unavoidable at long-time service. Z-phase particles that are formed grow quickly and consume the beneficial MX particles. The coarse Z-phase particles do not contribute to the creep strength of the steel and thus result in pre-mature failures [53].

The first strategy to tackle Z-phase formation was to delay this phase transformation as much as possible, but it was found that to delay this phase transformation, it is necessary to decrease the Cr content. The lower Cr content will not provide sufficient oxidation resistance for steam temperature of 650°C. Thus this strategy did not work.

Within the European COST 536 ACCEPT action, Danielson and Hald from the Technical University of Denmark proposed a novel alloy design concept, Z-phase strengthening [35]. The idea is to use the Z-phase precipitates as a thermodynamically stable strengthening agent. This means that the composition of the steel and the heat treatments are designed in such a way that a controlled nucleation of finely distributed Z-phase precipitates is achieved after heat treatment or in the early stages of the service, see **Figure 2.4**. Good creep resistance would be expected, if densely distributed fine Z-phase precipitates can be formed during heat treatment and if they coarsen slowly during service.

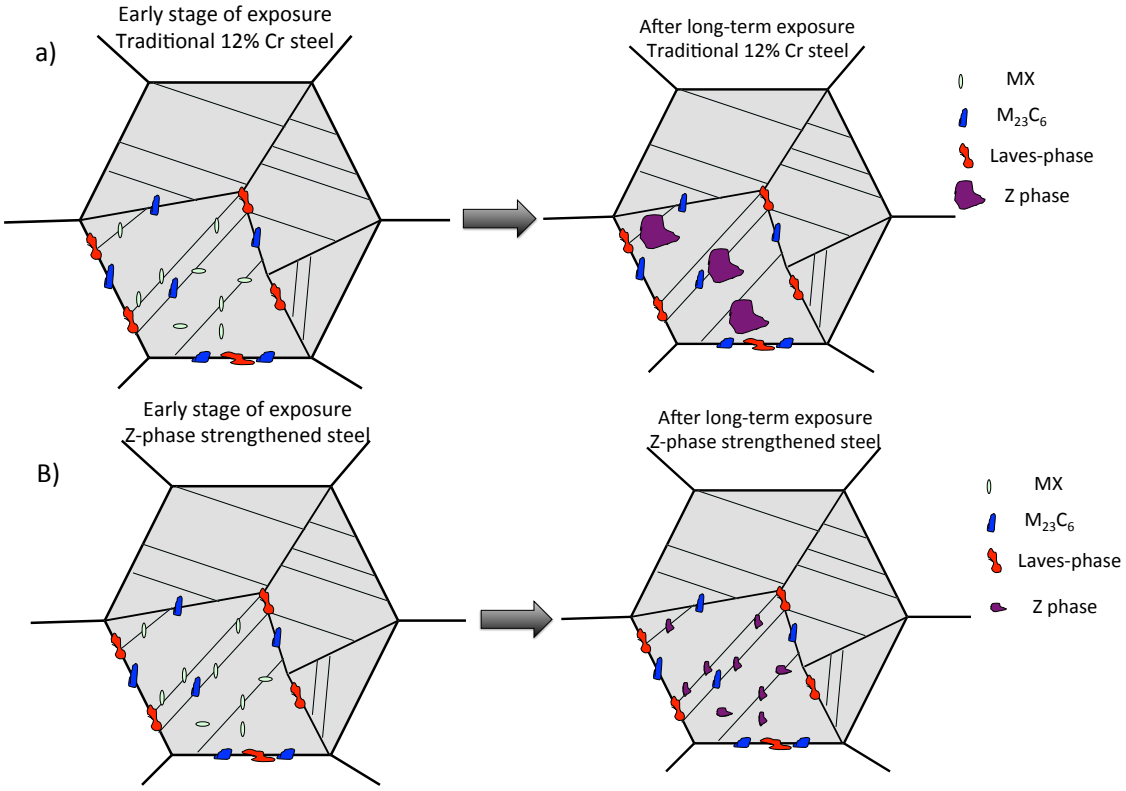

Figure 2.4 Schematic illustrations of a) traditional 12% Cr steels b) Z-phase strengthened steels.

Investigations of Z-phase precipitation rate at 600, 650, and 700°C has shown that in 12% Cr steel, Z-phase forms fastest at 650°C [77]; thus the steam temperature of 650°C as well as a high Cr content facilitate the formation of Z-phase.

To achieve a dense distribution of Z-phase, it is necessary to understand the precipitation behaviour of Z-phase. Z-phase does not nucleate on its own and there are two mechanisms discovered for Z-phase formation from precursor phases.

2.4.1 MX to Z-phase transformation

Cipolla et al. [77] has investigated the early stages of Z-phase formation in a model alloy (containing very low carbon content of 0.0048 wt.% and no Co) which was designed to form only modified Z-phase based on Cr(V,Nb)N. The MX precipitates found in the steel were divided in two categories of fine V-rich MN and larger Nb-rich MN precipitates.

In the aged specimens, Cr-rich MN precipitates were found, which were referred as hybrid particles. The composition profile of the hybrid particles showed a smooth transition from a Cr-rich rim to a Cr-poor zone in the centre of the particles, see **Figure 2.5**. The chemical composition of the rim was close to the composition of Z-phase and the composition of the core was close to the composition of MX. This indicated that Z-phase formation is closely related to MX precipitates and is a result of Cr diffusion from matrix to MX precipitates. For small precipitates less than 100 nm, the whole precipitate transformed to Z-phase while for bigger ones, Cr might not diffuse all the way to the core of the precipitates and thus transformation to Z-phase might occur locally [75, 77].

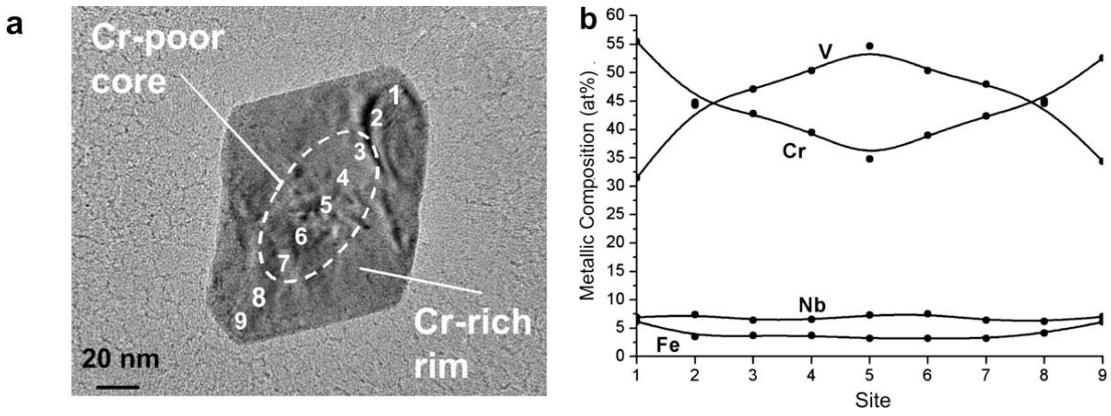

Figure 2.5 a) Hybrid precipitate with a Cr-rich rim and Cr-poor core. b) Energy Dispersive X-ray Spectroscopy (EDXS) results showing a smooth transition from the core to rim, with permission by Elsevier [77].

Thus as a result of the Cr uptake from the matrix by V-rich MN precipitates, Z-phase is formed. The proposed mechanism is schematically shown in **Figure 2.6**. The crystallographic transformation is believed to occur after the chemical transformation. Cubic MX transforms into cubic Z-phase, and it then transforms into tetragonal Z-phase. The cubic Z-phase is believed to be an intermediate structure between cubic MX and tetragonal Z-phase [75, 77].

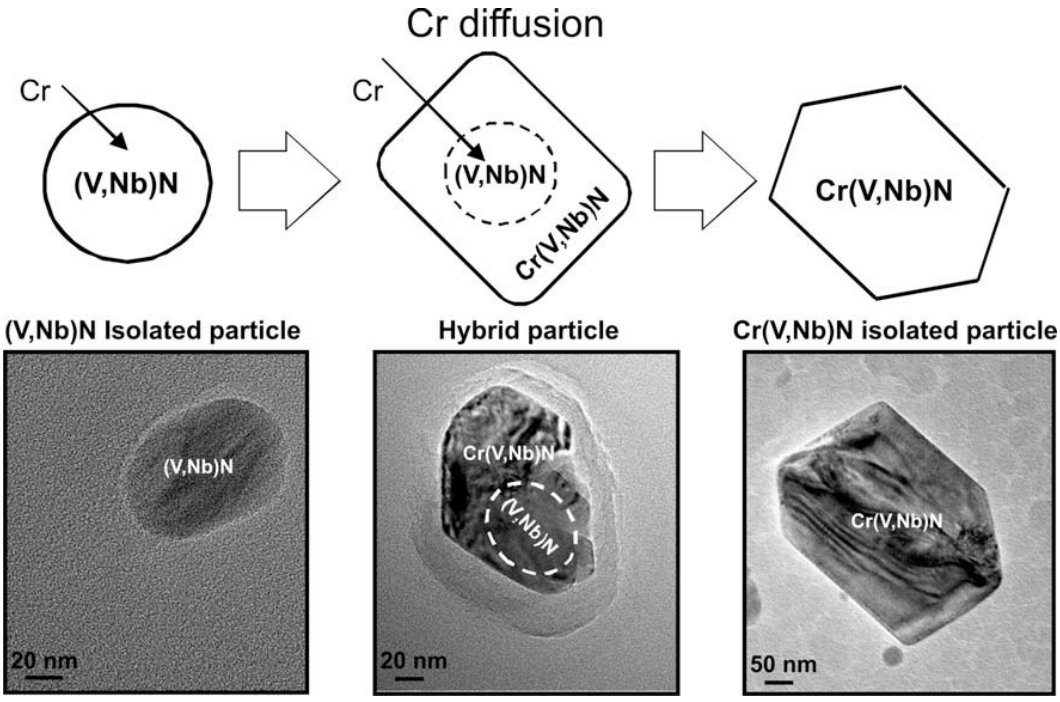

Figure 2.6 Formation of Z-phase from MX precipitates via Cr-uptake from matrix, with permission by Elsevier [77].

Cipolla also introduces a less straightforward mechanism to form Z-phase from the larger Nb-rich MN precipitates in the same steel as described above. Several Cr-rich regions were found on a large Nb-rich MN precipitate. Once the Cr regions are formed within the precipitate, Z-phase forms and grows via consuming V, Nb, and N from the host MN precipitate, probably through the ferrite matrix rather than the precipitate itself. This phase transformation from large Nb-rich MN precipitates lead to formation of several Z-phase precipitates as parallel precipitates [77]. The proposed mechanism and TEM micrographs are provided in **Figure 2.7.**

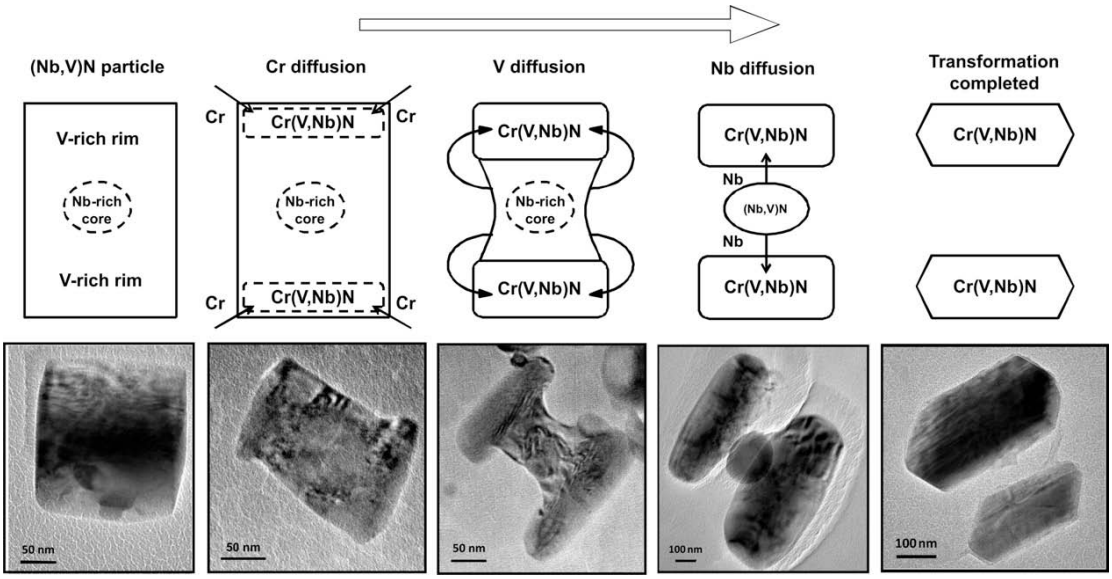

Figure 2.7 Formation of Z-phase from large Nb-rich MN precipitates during ageing at 650°C, starting from the left picture (as-treated condition) to the right picture (aged for 10,000 h), with permission by Elsevier [77].

2.4.2 M_2N to Z-phase transformation

Kim ET AL. [78] has investigated the formation of Z-phase from Cr_2N precipitates in an 11CrMoVNbN steel (containing 0.16 wt.% C, 0.06 wt.%N and no Co). It is reported that the V content of Cr_2N increased with ageing time at 593°C, while the composition of Nb(C, N) remained relatively intact during ageing process. After long-term ageing, the V content of the Cr_2N increased so that the composition of Cr_2N became very close to that of Z-phase.

The Energy Dispersive X-ray Spectroscopy (EDXS) investigation of a Cr_2N precipitate showed that there is a V-rich rim around the Cr_2N precipitate. Z-phase precipitates were also found adhered to Cr_2N precipitates in the longer aged specimens. Based on these observations, and similar composition of the rim of the Cr_2N as of Z-phase, it was proposed that Z-phase could nucleate on the rim of Cr_2N precipitates, where V is enriched [78]. Considering the presence of adhered Cr_2N to coarse Z-phase precipitates after long-term ageing, it is suggested that the Cr_2N precipitate does not transform to Z-phase, but Z-phase nucleates and grows at the rim of the Cr_2N precipitates. The proposed mechanism for Z-phase formation from Cr_2N is schematically described in **Figure 2.8.** It was suggested that a high N content in the investigated steel resulted in formation of Cr_2N, which then provided the nucleation site for Z-phase precipitates [78].

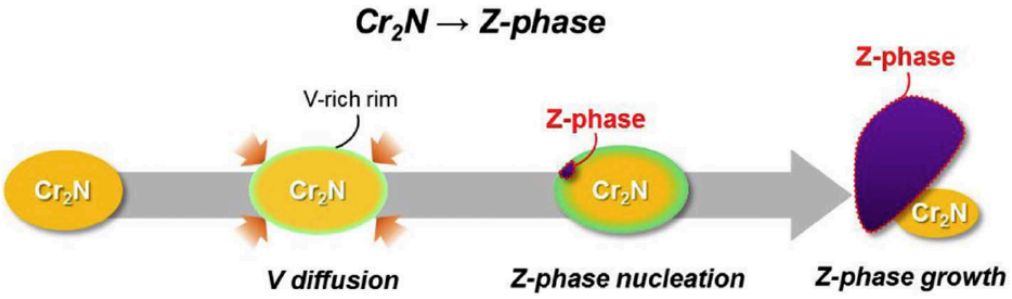

Figure 2.8 Schematic drawing of the formation of Z-phase from Cr_2N, with permission by Elsevier [78].

2.4.3 Strategy for alloy development

Martensitic 9–12% Cr steels are very complex materials and their alloy development requires optimization of 10–12 alloying elements. The strategy for such an alloy development is based on materials modeling as well as experimental trials. The effects of alloying elements on the microstructure and mechanical properties are discussed below.

Chromium

Based on the thermodynamic model proposed by Danielsen and Hald [54] and experimental observations [77], a high Cr content of 11–12% is required to accelerate the phase transformation from MX to Z-phase in Z-phase strengthened steels. However, one possible problem with such a high Cr steel is the formation of δ-ferrite. δ-ferrite in these steels reduces creep strength and toughness and thus must be considered in alloy development [24]. The Cr equivalent (Cr_{eq}) value is mostly used as a measure of the possibility for formation of δ-ferrite during solidification of alloy. To avoid δ-ferrite formation, the Cr_{eq} value must be less than 10. The Cr_{eq} is calculated by the following equation [79]:

$$Cr_{eq} = Cr + 0.8Si + 2Mo + 1W + 4V + 2Nb + 1.7Al + 60B + 2Ti + 1\,Ta - 20C - 20N - 2Ni - 0.4Mn - 0.6Co - 0.6Cu\ (wt.\%) \quad \textbf{Equation 2-3}$$

A high Cr content also provides sufficient oxidation resistance in this family of steels and especially for 650°C steam temperature, a high Cr content of 11–12% is required. Moreover, in 12% Cr steels, Z-phase forms faster at 650°C and hence such a high Cr content can lead to a faster formation of Z-phase, which is required for Z-phase strengthened steels [35, 80].

Nitrogen

Nitrogen martensite has a morphology similar to that of the carbon martensite. At low N levels, formation of a lath martensite is expected [81]. Nitrogen is well known for increasing the hardenability of steels with low carbon content. Nitrogen contributes to the formation of martensite structure in Z-phase strengthened steels when the C content is limited. Besides, N is a necessary element in formation of Z-phase. Care must be taken in defining the N content. Too high N content may result in the formation of porosities in the cast material. An excess N in relation to the nitride formers (such as Ta, Nb, and V) may also result in the formation of Cr_2N in addition to MX [82].

Carbon

Too much carbon promotes the formation of $M_{23}C_6$ instead of MX precipitates. Consequently, not only Cr is consumed by $M_{23}C_6$ and less Cr is left in the matrix for Z-phase formation, but also a fine distribution of MX cannot be obtained. Since one possible path to form Z-phase is via MX precipitates, a fine distribution of MX is necessary in Z-phase strengthened steels. Too high carbon content also results in formation of TaC or NbC, which do not transform to Z-phase.

Niobium, tantalum, vanadium

In Z-phase strengthened steels, a quick phase transformation from fine MX to Z-phase is required. V, Nb and Ta are Z-phase forming elements. The formation of V-based Z-phase is slow [35] compared to Nb-based and Ta-based Z-phase precipitates. Nb-based Z-phase results in coarse precipitates compared to the Ta-based Z-phase [83]. Thus, Ta seems to be the appropriate candidate to provide a fine distribution of Z-phase.

Other alloying elements

Tungsten is added to provide further solid solution hardening and precipitate hardening by forming Fe_2W Laves-phase. However, too high content of W might result in formation of δ-ferrite and reduction of toughness. Mn, Ni, Co and/or Cu are added to the steel to suppress the formation of δ-ferrite. Too high content of these alloying elements reduces the ability to temper the alloy at high enough temperatures. Co is believed to enhance the Z-phase formation [35]. Co is the only element that increases the M_s temperature without increasing retained austenite after austenitization treatment in 9–12% Cr steels [84]. Co also slows down the diffusion of atoms in metals. The diffusion of atoms depends on their magnetic interaction that increases below the Curie temperature, and Co increases the Curie temperature of the steels [85].

Boron is added to the steel to improve the hardenability. B addition to the steel decreases the rate of Ostwald ripening of $M_{23}C_6$ and thus enhances the precipitation hardening [43, 86]. The B and N contents must be carefully designed during alloy development since it might result in formation of massive BN particles at high temperatures [11, 87]. Therefore, less N is left in the matrix for precipitation of Z-phase.

Chapter 3

Experimental methods

There is no such a thing as failed experiment, only experiments with unexpected outcomes.

Richard Buckminster Fuller
Author 1895-1983

The experimental investigation in this thesis was mainly aimed at understanding the precipitation reactions and phase transformations during heat treatment and ageing. Several trial steels in the as-tempered condition and aged/crept conditions were characterized carefully. To obtain reliable results on the chemistry of the precipitates, their morphology and crystal structure, a number of techniques and sample preparation methods were employed. Scanning electron microscopy (SEM) was mainly used to obtain an overview of the microstructure of 9–12% Cr steels in the as-tempered condition; transmission electron microscopy (TEM) was mainly used to study the precipitates, their chemistry, and their crystal structure, and atom probe tomography (APT) was the main technique used to determine the chemistry of precipitates as well as the matrix.

3.1 Studied materials

In this thesis, seven Z-phase strengthened martensitic 11–12% chromium steels were studied. The chemical compositions of these trial steels are presented in **Table 3.1**.

The trial steels are named based on their C content and Z-phase forming element(s), Ta and Nb.

Table 3.1 Chemical composition of investigated 12% Cr steels (Fe in balance).

Steel	Name in paper(s)		C	Si	Mn	Cr	Ni	Co	W	Cu	Ta	N	B	Other
ZNb-ULC	*P1 (Z-Nb)*	at.%	0.02	0.60	0.50	12.64	1.47	5.2	0.87	-	-	0.15	0.02	Nb 0.16
	PIII (Z-Nb)	wt.%	0.005	0.30	0.50	11.64	1.47	5.4	2.82	-	-	0.036	0.004	Nb 0.26
ZTa-ULC	*PII (CrTaN-steel)*	at.%	0.02	0.60	0.49	12.84	0.48	7.01	0.89	-	0.12	0.13	0.02	-
	PIII (Z-Ta) *PIV (Z-steel)*	wt.%	0.005	0.30	0.48	11.79	0.50	7.30	2.90	-	0.39	0.033	0.004	-
ZTa-XHC	*PIV (ZCuC-steel)*	at.%	0.28	0.62	0.22	13.13	0.18	3.35	0.76	1.73	0.11	0.20	0.03	-
	PVII (S1)	wt.%	0.06	0.31	0.21	12.10	0.19	3.50	2.47	1.95	0.36	0.049	0.006	-
ZTa-LC	*PV (ZLC)*	at.%	0.07	0.58	0.09	12.45	0.10	3.72	0.61	1.77	0.12	0.18	0.01	-
	PVII (S3-1)	wt.%	0.015	0.29	0.09	11.50	0.11	3.90	2.00	2.00	0.37	0.045	0.002	-
ZTa-MC	*PV (ZMC)*	at.%	0.13	0.68	0.12	12.1	0.17	2.66	0.61	1.76	0.10	0.18	0.02	-
	PVII (S2-1)	wt.%	0.028	0.34	0.12	11.2	0.18	2.80	2.00	2.00	0.35	0.045	0.004	-
ZTa-HC	*PV (ZHC)*	at.%	0.23	0.45	0.12	11.9	0.20	2.95	0.54	-	0.13	0.14	0.02	Mo 0.29
	PVII (S2-3)	wt.%	0.05	0.23	0.12	11.1	0.21	3.10	1.80	-	0.43	0.036	0.004	Mo 0.50
ZTaNb-MC	*PVI (Z-TaNb)*	at.%	0.14	0.64	0.13	12.1	0.16	3.1	0.64	1.9	0.06	0.17	0.03	Nb 0.10
	PVII (S2-2)	wt.%	0.03	0.32	0.13	11.2	0.17	3.2	2.1	2.1	0.19	0.042	0.005	Nb 0.16

The ZNb-ULC, and ZTa-ULC trial steels contain ultra low carbon (ULC) content of 0.005 wt.%. In the ZNb-ULC and ZTa-ULC trial steels, Nb and Ta are employed to form Z-phase, respectively. Both trial steels were produced in 80 kg ingots by vacuum induction melting. The ingots were hot rolled into 20 mm thick plates. Both steels were austenitized at 1150°C and quenched to room temperature. Both steels were investigated in the aged condition at 650°C for 24 (as-tempered), 1000, 3000, and 10,000 h. For ZTa-ULC, the creep tests were done on samples tempered either at 650°C for 24 h or 720°C for 6 h.

The ZTa-XHC steel contains the highest C content (XHC (Extra High Carbon)) amongst the trial steels investigated in this work, and Ta is employed to form Z-phase. ZTa-XHC was produced in 80 kg ingot by vacuum induction melting. The ingot was hot rolled into a 20 mm thick plate. It was then austenitized at 1150°C and quenched to room temperature. The steel then underwent double step tempering-first step at 650°C for 6 h, and second step at either 740°C or 700°C for 6 h.

Ta is used to form Z-phase in the trial steels of ZTa-LC (low carbon), ZTa-MC (medium carbon), and ZTa-HC (high carbon). Steel making at Saarschmiede GmbH, Völklingen, Germany, included vacuum induction melting and vacuum arc remelting, and ingots were forged to 40 mm × 40 mm square bars. The trial steels were then austenitized at 1100°C for 1 h, cooled in air to room temperature, and then double step tempered for 4 h at 650°C followed by 2 h at 750°C. All trial steels were investigated in the as-tempered condition and after 1000 h ageing at 650°C. ZTa-LC was also studied after 4000 h ageing at 650°C. ZTa-MC and ZTa-HC were as well investigated after 10,000 h ageing at 650°C.

In the ZTaNb-MC steel, both Ta and Nb are employed to form Z-phase. The steel contains medium carbon content and it was produced by induction melting and vacuum arc re-melting at Saarschmiede GmbH, Völklingen, Germany. The ingots were then forged to 40 mm × 40 mm square bars. The steel was austenitized at 1100°C for 1 h then quenched in air. The steel was then tempered at 650°C for 4 h and at 750°C for 2 h.

Moreover, three other trial steels were also produced that are referred to as S3-2, S3-3, and S3-4 in *Paper VII*. However, a detailed investigation of these trial steels has not been yet performed.

3.2 Scanning electron microscopy

SEM was mainly used to obtain an overview of the microstructure and image the grain structure, lath boundaries, and particles larger than 10 nm. The following short description of SEM is based on the book by J.Goldstein et al. [88]. The two major parts of an SEM are the electron column and the control console. In the electron column, electrons are emitted from an electron gun, nowadays often a field-emission gun, with an energy adjustable in the range of 0.1-30 keV. Electromagnetic lenses control the path of electrons in the column with a pressure of roughly one billionth of atmospheric pressure. The control console contains a viewing screen, knobs and computers that control the beam.

The electrons emitted from the electron gun are accelerated to a high energy. They travel through electromagnetic lenses and form a focused electron beam on the specimen. Electrons interact with the specimen and different signals are generated from the so-called electron-material interaction volume. The size of interaction volume plays an important role in interpreting the results obtained from SEM. Different parameters such as the accelerating voltage, the atomic number of elements in the specimen and density of the specimen affect the interaction volume size. Scanning coils in the column deflect the beam in X and Y direction over a rectangular area on the specimen surface. The generated signals from the interaction volume are then recorded by different detectors for each beam position and form a two-dimensional image of the specimen.

Secondary and backscattered electrons and characteristic X-rays are the major signals produced within the interaction volume. Secondary electrons (SEs) are used to obtain topographical images of the specimen since the possibility of emitting SEs from the edges is higher compared to the flat areas on the specimen surface. SEs are produced by inelastic scattering of the incident beam and have low energies. Backscattered electrons (BSEs) are produced by elastic scattering of the incident electrons within the interaction volume. BSEs have energies close to the energy of the incident electrons. BSEs carry information on the composition of the specimen. By considering the fact

that the probability of elastic scattering increases by increasing the atomic number, Z, it is possible to obtain images with compositional contrast of the specimen. Areas containing heavier elements produce more BSEs, resulting in higher intensities compared to the areas containing light elements in the image. The third important signals produced within the interaction volume are characteristic X-rays, which are discussed in more detail in section 3.4. **Figure 3.1** summarizes different signals and detectors in a SEM.

In this thesis, BSEs and X-rays are often used for characterization of different particles. Laves-phase contains W which is a heavy element and thus it gives a very bright contrast compared to $M_{23}C_6$ and Cu particles by using BSE imaging. MX and Z-phase particles also contain a heavy element, Ta, and thus BSEs are often used to show the distribution of these particles within the steel matrix. The difference between the contrast of Z-phase and Laves-phase in BSE imaging is so small that one needs to employ EDXS to distinguish between these particles.

Figure 3.1 Schematic drawing showing the electron source, different signals and frequently used detectors in an SEM.

The SEM results presented in this thesis were obtained using a Zeiss Ultra 55^{TM} SEM operated at accelerating voltages ranging from 2 to 15 kV. The energy and angle Selective Backscattered (EsB) detector in the SEM provides the possibility to obtain high-resolution backscattered electron images that can clearly reveal precipitates of nanometre size. When the SEM is operated at a rather low accelerating voltage, the low energy loss electrons that carry chemical information from the very surface (a few nanometres) of the material can be collected by this EsB detector installed inside the electron column. This gives a SEM micrograph with chemical information and a resolution as high as 10–20 nm, which is much better compared to the resolution of traditional BSE detectors, 0.5 micron.

3.3 Transmission electron microscopy

A TEM consists of an electron gun, electromagnetic lenses, and a viewing screen that are all enclosed in a vacuum system. The accelerating voltage in a TEM, 100–300 kV, is much higher compared to that in a SEM, maximum 30 kV. The specimen has to be electron transparent meaning that the electrons emitted from the gun have to pass through the specimen. Thus in a TEM, the transmitted electrons from an ultra thin specimen (thickness <100nm) are detected and used for imaging [89]. **Figure 3.2** schematically shows a TEM.

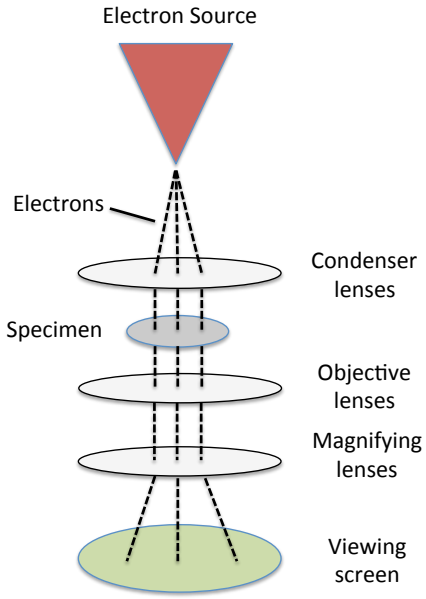

Figure 3.2 Schematic drawing showing the electron source, electromagnetic lenses, specimen, and viewing screen in TEM.

The incoming electron beam interacts with the specimen and results in elastically (no loss of energy) and inelastically (losing their energy) scattered electron, and X-rays. The obtained contrast in the TEM mode and the intensity distribution in diffraction patterns mainly result from elastically scattered electrons. Electron diffraction is a powerful technique that is used to identify the crystal structure. Inelastically scattered electrons mostly provide information on the chemistry of the specimen. Energy-loss electrons and X-rays are often used to collect information on the chemistry of the material.

In the bright field (BF) mode of TEM, the objective aperture is inserted in the back focal plane of the objective lens, and only the direct beam passes through the aperture. The acquired image is a result of weakening the transmitted beam by its interaction with the specimen. Mass-thickness and diffraction contribute to the contrast of image. Areas containing heavy elements and thick areas appear with a dark contrast. Areas with different crystal structure provide different contrast in the image (see **Figure 3.3 a**).

In the Scanning Transmission Electron Microscopy (STEM) mode, the electron optics is similar to that in a SEM. The electron beam is focused on the plane of the specimen and scans over the specimen. In the STEM mode compared to SEM, instead of SEs and BSEs, the transmitted electrons through the electron transparent specimen are used to form images. A so-called High-Angle Annular Dark-Field (HAADF) detector provides an image with Z-contrast (Z: atomic number). The areas with greater Z

and/or thickness scatter electrons more strongly and thus they appear brighter using HAADF, see **Figure 3.3 b**.

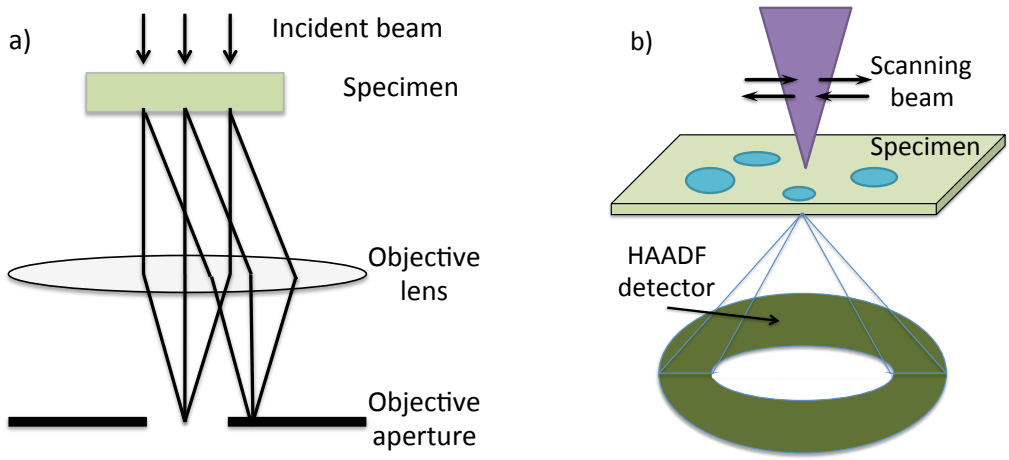

Figure 3.3 Schematic drawing showing a) the bright field imaging mode in TEM b) the STEM mode.

There are generally two ways to produce diffraction pattern in the TEM; using the selected area aperture to form selected area diffraction pattern (SADP) or by using a convergent beam to form convergent beam electron diffraction (CBED). Since the smallest SAD aperture (100 nm) was bigger than the size of precipitates (around 50 nm), to avoid any contribution from the matrix to the diffraction pattern of the precipitates, CBED was mainly employed to characterize the precipitates.

In this thesis, imaging was done in both TEM and STEM modes. Moreover, EDXS and diffraction patterns of precipitates were collected to identify the type and crystal structure of precipitates. Two TEMs were employed, a FEI Tecnai T20 TEM equipped with a LaB_6 gun operated at 200 kV, and a FEI Titan 80-300^{TM} (S)TEM, equipped with a Schottky field emission gun, operated at 300 kV.

3.4 Energy dispersive X-ray spectroscopy

The incoming electrons interact with the specimen in both SEM and TEM and create characteristic X-ray radiation by ionizing atoms in the specimen. An electron from a higher energy state in an ionized atom falls to a lower energy state and the energy difference can result in X-ray radiation. Since the difference in energy between two electron shells is unique for each atom, X-rays of characteristic energies are used for analysis. The emitted X-rays are collected using a detector mounted above the specimen. Analyzing the intensity distribution of X-rays as a function of energy tells you which elements that are present in the material and their concentration. The

obtained information from EDXS can be treated both quantitatively and qualitatively. The simplest way to acquire EDXS is to position the electron beam on the feature of interest and acquire a spectrum (spot analysis). It is also possible to collect the EDXS spectra while scanning the electron beam over the specimen (EDXS mapping), which provides elemental mapping of the material.

3.5 Atom probe tomography

APT is by far the most powerful analytical method to study the chemical composition at an atomic level. It determines the chemical composition based on counting the number of atoms of each type. APT is an instrument capable of determining the species of a single atom from the surface of a needle-shape specimen. A needle-shaped specimen with a tip radius of less than 50 nm is subjected to a very high positive DC voltage in an ultra-high vacuum chamber ($\approx 10^{-9}$ Pa) at cryogenic temperatures (20–100 K). An additional voltage or laser pulse is superimposed on the specimen and results in a controlled ionization of surface atoms of the needle; this process is called field evaporation. This method is destructive in nature and the ionized atoms leave the surface of the specimen and are accelerated towards a position sensitive detector through a circular aperture that is held at zero potential and serves as a counter electrode, see **Figure 3.4**. The position sensitive detector registers the coordinates (X and Y) of the atomic or molecular ion. The time of flight starting from the superimposed pulse until the ion reaches the detector is measured and by considering that only the surface atoms are ionized, gives the possibility to evaluate the spatial position and atomic mass for each ion. Thus a 3-dimentional reconstruction of the tip can be created.

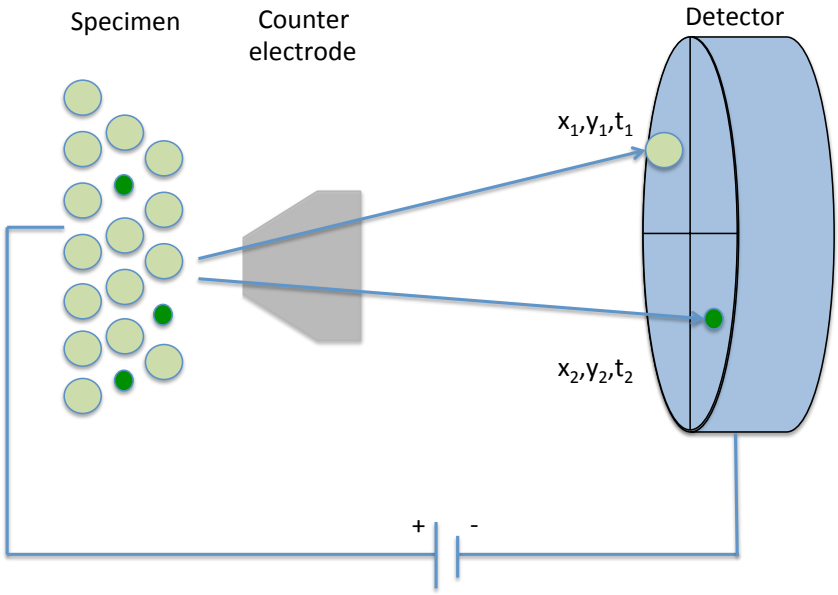

Figure 3.4 Schematic drawing of experimental setup in the APT.

An APT measurement of a suitable specimen can contain tens of millions of atoms in a volume of 100×100×500 nm^3. Each event on the detector is registered via two coordinates as well as a time of flight and processing this huge amount of data requires a proper computing power.

An Imago LEAP 3000X HR local electrode APT was employed to study the chemical composition of precipitates. During analysis the specimen was held at a temperature of 55–60 K. The instrument was operated in pulsed laser mode with a laser pulse energy of 0.3 nJ. The data collected by the instrument was further analyzed using the IVAS 3.4.6 software.

3.6 X-ray powder diffraction

X-ray diffraction (XRD) is generally used for identification of crystalline phases, where X-rays pass through a crystal and give rise to diffraction patterns based on the Bragg's law [90]. The X-ray powder diffraction technique is used to characterize samples in the form of powders. Considering the relatively low volume fraction of precipitates in 9–12% Cr steels, one needs to extract the precipitates from the matrix in the form of a powder. The extraction of precipitates was done electrolytically through dissolving the steel matrix, which does not dissolve the precipitates. To achieve enough precipitates in the form of powder for XRD measurements, at least a few grams of the matrix need to get dissolved. The precipitate extraction and XRD measurements were done at Sandvik Materials Technology.

3.7 Specimen preparation

Several specimen preparation methods can be employed for microstructure investigation of steels. Each method might introduce some artefacts and it is very important to identify these artefacts for a proper understanding of the microstructure. We have employed three different methods of sample preparation: mechanical polishing, electropolishing, and ion milling.

Specimen preparation for electron microscopy

Mechanical grinding and polishing is the most common method that was employed to prepare specimens. This relatively easy and quick method provided specimens good enough for a SEM investigation. However, the surface of the specimen often contained scratches induced by this preparation technique.

For electropolishing, the specimen needed to undergo first mechanical polishing and then chemical polishing. An electrolyte of 10% perchloric acid in methanol was used at -30°C to electropolish disks (3 mm in diameter and 100–200 μm thick) using a Struers Tenupol Twin Jet electropolisher until perforation. The area adjacent to the hole was very thin (<100 nm) and was used for TEM investigations. By considering the fact that electropolishing provides damage free and smooth surfaces, the electropolished specimens were also used for SEM investigations. However, with this method, Cu particles were dissolved in the electrolyte during electropolishing and holes were left in the matrix.

Ion milling and polishing is the most time-consuming method compared with aforementioned techniques. A Fischione low angle ion milling and polishing system was employed to prepare TEM specimens with large electron transparent areas. In this technique, emitted argon ions from ion sources are used for milling the 3 mm diameter disks. Compared to electropolishing, preparing specimens by ion milling has the advantage of leaving Cu particles intact for TEM analysis. This method also provides better specimens for SEM analysis using BSE detector. However, SE micrographs show a wavy surface as a result of prolonged ion milling.

Specimen preparation for APT

To produce a needle-shaped specimen from metallic rods, electropolishing was employed. First a low speed saw was used to cut slices of 0.3 mm from a bulk specimen. Then rods of the size $0.3\times0.3\times15$ mm^3 were cut using the same saw. Rods were mounted in small aluminum holders with a 0.5 mm hole. Then electropolishing was done in two steps as shown in **Figure 3.5**. In the first step, a thin layer of electrolyte containing 10 vol.% perchloric acid in 2-butoxyethanol floated over trichloroethylene (inert liquid). Then by applying a voltage, a neck was created in the part of the material that was immersed in the electrolyte. In the second step, the whole

specimen was placed in a weaker electrolyte, 2 vol.% perchloric acid in 2-butoxyethanol, and slow polishing continued until the lower part of the specimen dropped and two sharp needles were created.

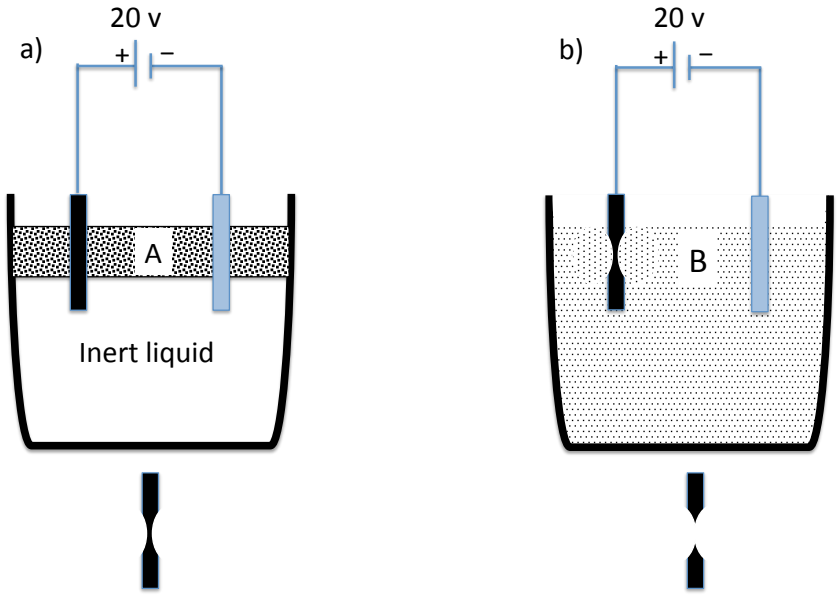

Figure 3.5 Schematic showing two-step electropolishing to produce APT specimens. a) Stage 1 to produce a neck in the specimen, electrolyte A is 10 vol.% perchloric acid in 2-butoxyethanol, b) Stage 2 to obtain a sharp needle, electrolyte B is 2 vol.% perchloric acid in 2-butoxyethanol.

3.8 Mechanical testing

The toughness of the trial steels in the as-tempered condition was evaluated using Charpy impact test at room temperature in accordance with standard ISO 148–1:2009, using a 2 mm depth V-notch. At least three specimens were tested and the average absorbed energy was reported.

The creep rupture testing was performed in accordance with Standard EN ISO 204:2009. The creep rupture tests were carried out at 650 °C under a constant load corresponding to 120, 100, or 80 MPa using specimens of 7 mm in diameter, 50 mm in gauge length and 135 mm in total length.

Both creep and Charpy tests were done at Siemens Industrial Turbomachinery in Finspång.

Chapter 4

Summary of results and discussion

A good method of discovery is to imagine certain members of a system removed and then see how what is left would behave: for example, take away carbon from steel.

Inspired by Georg Christoph Lichtenberg
German Scientist (1742-1799)

In this chapter, the appended papers and manuscripts are summarized. The results and discussion parts are presented based on the important concerns for Z-phase strengthened steels: Z-phase formation, coarsening rate of Z-phase, impact toughness, the role of C on Z-phase formation, the preferred mechanism to form Z-phase, and formation of Z-phase based on the combination of Ta and Nb.

4.1 Z-phase formation

In Z-phase strengthened steel, first of all, it is required to study whether a fine distribution of Z-phase can be achieved in the as-tempered condition or the early stages of service. The chemical composition of ZTa-ULC and ZNb-ULC were designed in order to accelerate the formation of Z-phase. Both steels benefit from a

high Cr content, which not only provides a high oxidation resistance for the steels [71], but also accelerates the phase transformation from MX to Z-phase [35, 54]. The low C content in these trial steels suppressed the formation of carbides, which provided the possibility to study the strengthening effect of Z-phase precipitates without interference from carbides. Considering the limited amount of C (austenite stabilizer), a high amount of Co was required to balance between austenite stabilizers and ferrite stabilizers. Co is also beneficial for MX to Z-phase transformation as it reduces the affinity of Cr in the matrix and thus encourages in-diffusion of Cr to MX precipitates [35]. The Cr_{eq} value for ZNb-ULC and ZTa-ULC calculated based on equation 2.1 is approximately 8.2 and 9.2, respectively. The Cr_{eq} values are less than 10, and an electron microscopy investigation showed that no δ-ferrite was formed in the trial steels despite their high Cr content.

Extensive TEM work by researchers from the Technical University of Denmark has led to an understanding of the formation of Z-phase from MN precipitates; in-diffusion of Cr to MN precipitates. However, TEM is of limited accuracy in the composition measurement of such small precipitates that contain the light elements N and C. APT, capable of detecting all elements with equal sensitivity, provides the possibility of analyzing carbides and nitrides more accurately. However, these precipitates usually have a higher evaporation field compared to the steel matrix, which leads to an area of overlap on the detector where ions from both the precipitate and the matrix are detected. In *Paper I*, the formation of Z-phase was studied using APT and an accurate composition of the intermediate precipitates in ZNb-ULC steel was provided. Moreover, a method was developed to accurately measure the composition of small precipitates that suffer from local magnification artifacts using APT.

As Z-phase formation occurs by Cr diffusion into the MN precipitates, it is of great interest to investigate any concentration gradients in individual precipitates. There are three possible ways to analyze these small precipitates using IVAS^{TM} software: one-dimensional (1D) concentration profile, proxigrams, and iso-concentration surfaces. Using 1D concentration profile and proxigrams, important information on the distribution of alloying elements is achieved. However, to study complex systems such as carbides and nitrides in steels containing 10–12 alloying elements, care must be taken in interpreting the results due to the possible peak overlaps between different ions such as $^{56}Fe^{2+}$ and $^{14}N_2^+$, $^{28}Si^{2+}$ and $^{14}N^+$, and $^{54}Fe^{2+}$ and $^{54}Cr^{2+}$. In addition to the peak overlaps, the obtained data are disturbed by the local magnification effect.

Out of the three aforementioned techniques, it is only for the iso-concentration technique that there is a possibility to extract small volumes of ions and treat overlaps using the built-in peak deconvolution function and background subtraction in IVAS^{TM}. Normally, the iso-concentration value is selected in a way that the least contribution from matrix is involved, however by doing this lots of ions belonging to the precipitate are not measured, and only the composition of the core of the precipitates are considered as the composition of the whole particle, see **Figure 4.1**.

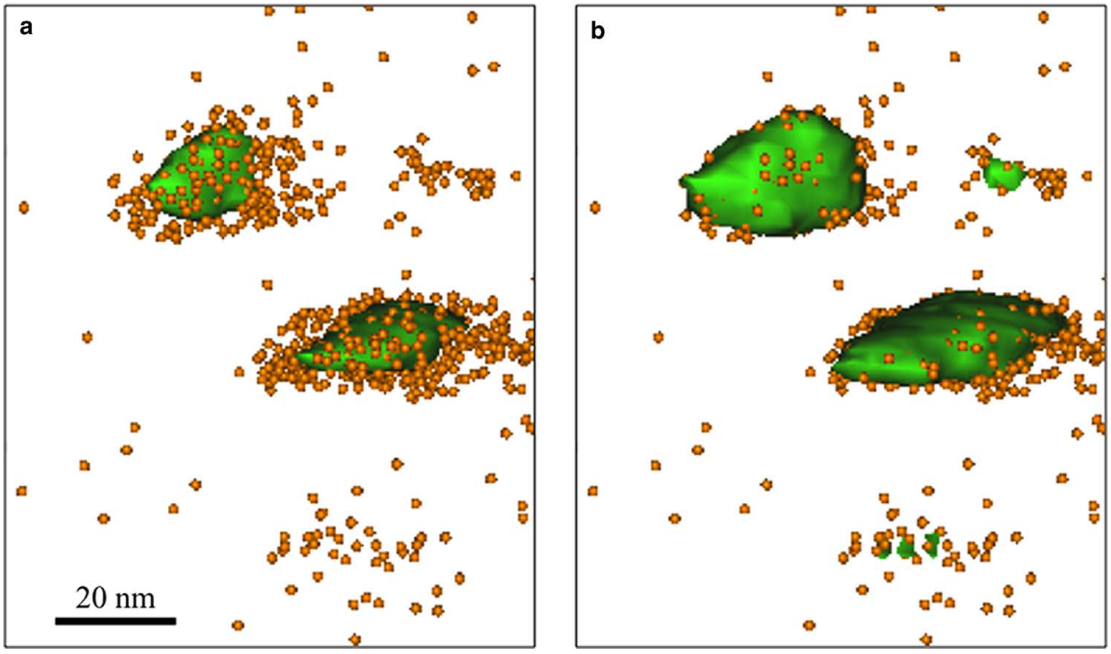

Figure 4.1 Iso-concentration surfaces with a volume, within which the concentration of Nb + Cr +N (**a**) >30 at% and (**b**) >20 at%. Brown dots represent $NbN^{1+,2+,3+}$ ions, which belong to the precipitates. With a higher concentration value, more ions from the outer part of the precipitate are excluded. The atom probe tomography data set is obtained from the ZNb-ULC steel aged for 24 h at 650°C (from *Paper I*).

To accurately measure any concentration gradients in individual precipitates, a routine explained in *Paper I* was employed to exclude the contribution from matrix to the composition of the precipitate. Using iso-concentration surfaces with different values and subtracting the matrix contribution based on "Co correction" and "Fe correction" enabled us to measure the composition of different layers of a precipitate revealing the core-shell structure of the transient precipitates between MX and Z-phase in the ZNb-ULC steel. **Figure 4.2** shows the composition of the precipitates layer by layer in the specimens aged for 24, 1005, and 3,000 h at 650°C. The Cr concentration in the core of the precipitate in the 24 h aged specimen is 20 at.% and in the outer shell of the precipitate reaches to 30 at.%. The in-diffusion of Cr continues during thermal ageing. After 3000 h ageing, the MX to Z-phase transformation is completed and the core and the shell of the precipitate have the same composition.

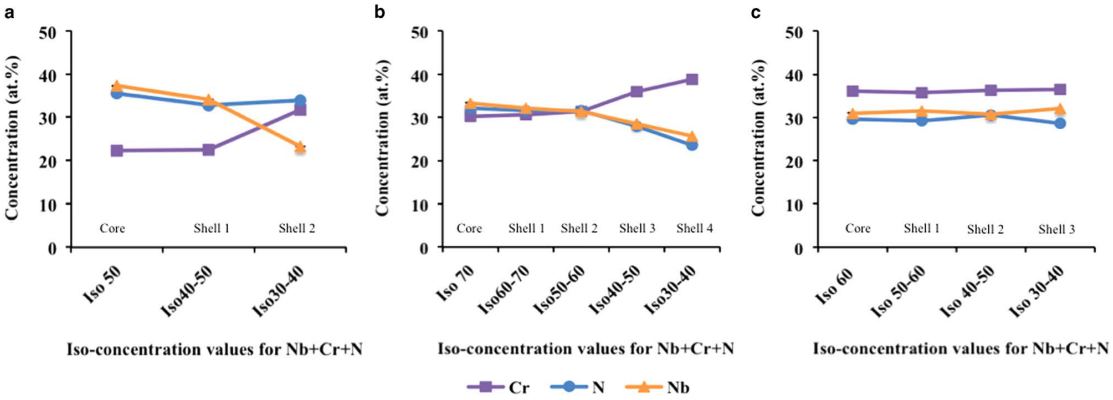

Figure 4.2 The composition of the core and the shells of the precipitates in the ZNb-ULC trial steel aged for (**a**) 24, (**b**) 1005, (**c**) 3000 h at 650°C obtained using the **"**Fe correction**"** technique on different iso-concentration surfaces. **"**Iso x–y**"** means a shell between the iso-concentration surfaces of Nb + Cr +N **>x**% and Nb + Cr +N **> y**% was analyzed. The non-visible error bars (1 SD) are smaller than the data point symbols (from *Paper I*).

In *Paper I*, it was shown that a combination of high Cr, Co, and ultra low carbon content can accelerate the formation of Z-phase in a Nb-based Z-phase strengthened steel. In *Paper II*, the obtained results on the Ta-based Z-phase was reported together with the creep results obtained for the ZTa-ULC steel showing the contribution of Z-phase to the creep strength at 650°C.

In *Paper II*, the ZTa-ULC steel was studied after ageing at 650°C for 24 (as-tempered), 1005, and 10,000 h. The creep tests at 650°C were done on two heat treatment conditions, either tempered at 650°C for 24 h or 720°C for 6 h. The PAG size in this trial steel was determined to be approximately 114 µm.

Figure 4.3 shows the creep strength versus the rupture time curve at 650°C for ZTa-ULC in comparison with two of the most widely used 9% Cr steels today, ASTM P91 and P92. It should be noted that the application temperature of P91 and P92 are below 650°C. The creep rupture strength of ZTa-ULC is better than P91 and close to P92, despite its much higher Cr content. It is worth noting that due to the absence of $M_{23}C_6$ (ultra low carbon in the steel), and as electron microscopy investigation showed, the precipitation hardening from Z-phase precipitates contribute to the strength of the ZTa-ULC steel.

APT investigation on the ZTa-ULC specimens aged at 650°C for 24 h showed that Ta and N contents in the matrix is almost zero meaning that the full volume fraction of nitrides has precipitated out. It is worth mentioning that part of the N and Ta segregated to the boundaries. **Figure 4.4** shows a TaN-molecular ion map from an APT reconstruction for ZTa-ULC aged for 24 h at 650°C. The same routine as described in *Paper I* was employed to accurately measure the composition of these small precipitates. The obtained composition showed the presence of Z-phase, as well as precipitates with a chemistry close to CrN, and Cr_XNTa (>50 at.% Cr, and 10–15

at.% of N and Ta). The precipitates were found in the form of thin blades in APT investigation. TEM studies of the specimens aged for 3000, and 10,000 h showed that Z-phase coarsens during isothermal ageing, keeping its blade-like morphology. The electron diffraction pattern obtained from Z-phase precipitates in the specimen aged for 1005 h showed that Z-phase has a more ordered tetragonal crystal structure.

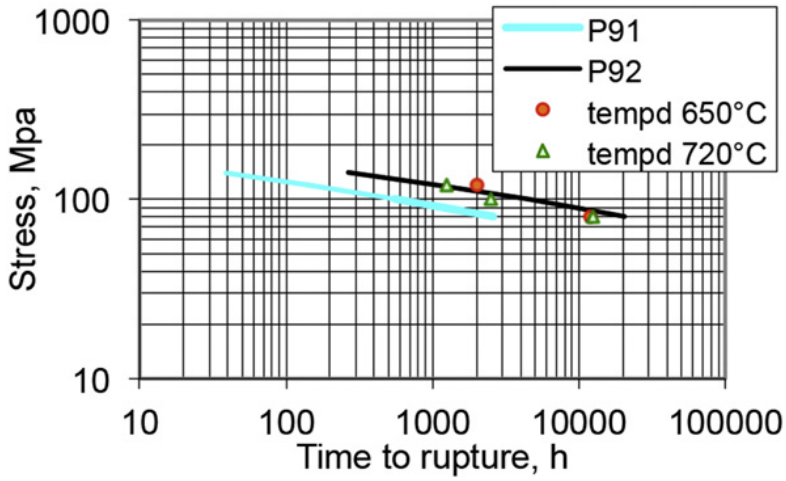

Figure 4.3 Creep rupture strength at 650°C for ZTa-ULC, either tempered at 650°C for 24 h or at 720°C for 6 h, in comparison with P91 and P92 (from *Paper I*).

Figure 4.4 Reconstruction of an APT data set obtained from the ZTa-ULC steel in the as-tempered condition (24 h aged at 650°C). Red dots represent TaN ions. The matrix ions are not shown for visual clarity (from *Paper IV*).

4.2 Coarsening rate of Z-phase

In *Papers I and II*, it was shown that by adjusting the composition of the steel, it is possible to accelerate the formation of Z-phase and hence a dense distribution of Z-phase was formed in the early stages of the heat treatment. It is then important to

investigate the coarsening behavior of Z-phase precipitates at the temperature of interest, 650°C, for both Ta-based and Nb-based Z-phase.

In *Paper III*, TEM was employed to investigate Z-phase evolution in the ZNb-ULC and ZTa-ULC steels. Both steels were austenitized at 1150°C for 1 h and aged for 1000, 3000, and 10,000 h at 650°C. Besides, in order to study the effect of strain on Z-phase evolution, a crept specimen of ZTa-ULC was investigated. The specimen was austenitized at 1050°C for 1 h and tempered at 700°C for 7 h before creep testing at 80MPa/650°C for 6311 h.

Moreover, Thermo-Calc software [91], with the thermodynamic database TCFE8 [92] and the mobility database MOBFE3 [93] was employed to calculate the chemical diffusivity and the influence of Co on the diffusivity of Ta and Nb in the Fe bcc matrix at 650°C.

Experimental coarsening rate of Z-phase

Z-phase precipitates were mainly found in blade-like morphology, see **Figure 4.5**. There are two commonly used methods to measure the size of precipitates in 9–12% Cr steels: particle diameter (PD) and equivalent circle diameter (ECD) [94– 96]. Considering that these two approaches give similar result as shown in Ref. [38], PD was selected as one of the methods to measure the size of Z-phase precipitates in this study. Besides, due to special morphology of Z-phase, another method was also employed, i.e. the equivalent sphere radius (ESR) of the precipitates.

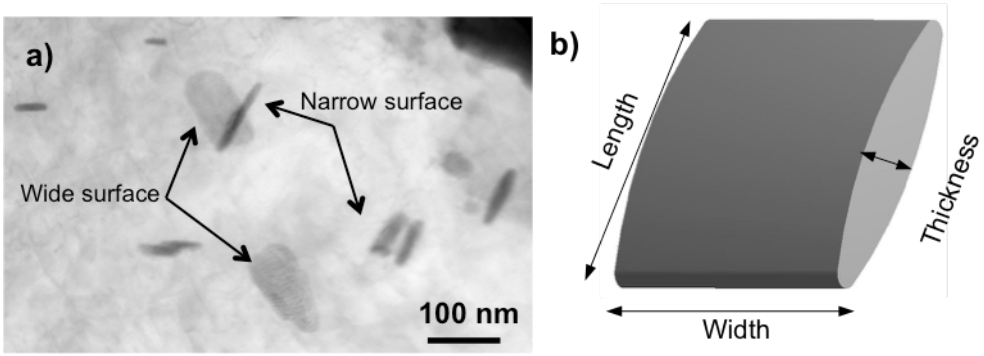

Figure 4.5 STEM/BF micrograph of ZTa-ULC steel aged for 10,000 h at 650°C showing the typical morphology of Z-phase precipitates in TEM images and b) a schematic drawing showing the morphology of Z-phase precipitates in three dimensions (from *Paper III*).

Both PD and ESR methods show similar results for the size evolution of Z-phase precipitates in both trial steels. There is a rapid increase in the size of the precipitates from 1000 h aged specimens to 3000 h aged ones. The fluctuation in the composition of the precursor precipitates to Z-phase and dissolution and transformation of precipitates are probably the main reasons for such a rapid increase in the size of Z-

phase precipitates in both steels. Thus, it was assumed that the increase in the size of the precipitates in this period belongs to the growth stage. Therefore, the coarsening rate for Z-phase precipitates is measured for the precipitate size evolution from 3000 h to 10,000 h ageing at 650°C in order to exclude the growth stage. The Ostwald ripening equation for the Z-phase size evolution from 3000 h to 10,000 h gave the following coarsening constant values: 1.4×10^{-30} and 2.8×10^{-31} (m^3s^{-1}) for the Nb-based and Ta-based Z-phase, respectively. The obtained coarsening constant is comparable to the coarsening rate of VN precipitates in P92 at 650°C calculated from the data presented in Ref. [95].

Calculated coarsening rate of Z-phase

Due to the limitation on the thermodynamical database for Ta-containing steels, a full kinetic modeling of Z-phase coarsening (using e.g. DICTRA software) is not possible. However, the coarsening constant can be calculated using the model by Ågren et al. [97]. An accurate composition of Z-phase precipitates (from APT), diffusivity of Nb and Ta (Thermo-Calc) in the matrix, interfacial energy of Z-phase (estimations from DFT calculations), and solubilities of Nb and Ta in the matrix (from APT) were fed into the Ågren's equation and coarsening constant of $K_P=1.11\times10^{-30}$ (m^3s^{-1}) for Z-Nb and $K_P=1.04\times10^{-31}$ (m^3s^{-1}) for Z-Ta were calculated.

Both experimental and theoretical coarsening constants show that Ta-based Z-phase coarsens much slower compared to the Nb-based Z-phase during isothermal ageing at 650°C. The experimental coarsening constant for Z-Nb was determined to 1.4×10^{-30} (m^3s^{-1}) and for Z-Ta to 2.8×10^{-31} (m^3s^{-1}), a factor of 5 smaller. The theoretical coarsening constant for Z-Nb is only slightly smaller than the experimental one, whereas the theoretical constant for Z-Ta is considerably smaller (a factor of 2.7) than the experimental one, suggesting that the experimental coarsening constant represents a mixture of growth and coarsening. The measured solubility of Nb and Ta in the steel matrix (20.5 at. ppm Nb and 17.4 at. ppm Ta) are close to each other. The estimated interfacial energy based on the Z-phase and matrix misfit is also not very different from each other. Thus, the smaller diffusivity of Ta in the steel matrix compared to that of Nb is believed to be the main reason for the lower coarsening rate of the Ta-based Z-phase.

A comparison between the size of Z-phase precipitates in the gauge and grip portions of a crept specimen showed that Ta-based Z-phase coarsens faster in the gauge portion, which is strained, compared to the grip portion, which is stress-free and not deformed.

4.3 Impact toughness

In a multi-phase system such as 9–12% Cr steels, where a combination of 10–12 alloying elements contribute to the formation of several precipitate phases, it is

important to investigate the role of small adjustments in the materials chemistry on the behavior of other phases and eventually the obtained mechanical properties.

Both ZNb-ULC and ZTa-ULC have low impact toughness, 2 and 3 J, respectively. Electron microscopy investigations showed the presence of continuous Laves-phase films at PAGBs for ZTa-ULC in the as-tempered condition, see **Figure 4.6 a**. Further studies of an impact-tested specimen showed that cracks follow the PAGBs where the continuous film of Laves-phase was present, see **Figure 4.6 b** and **c**.

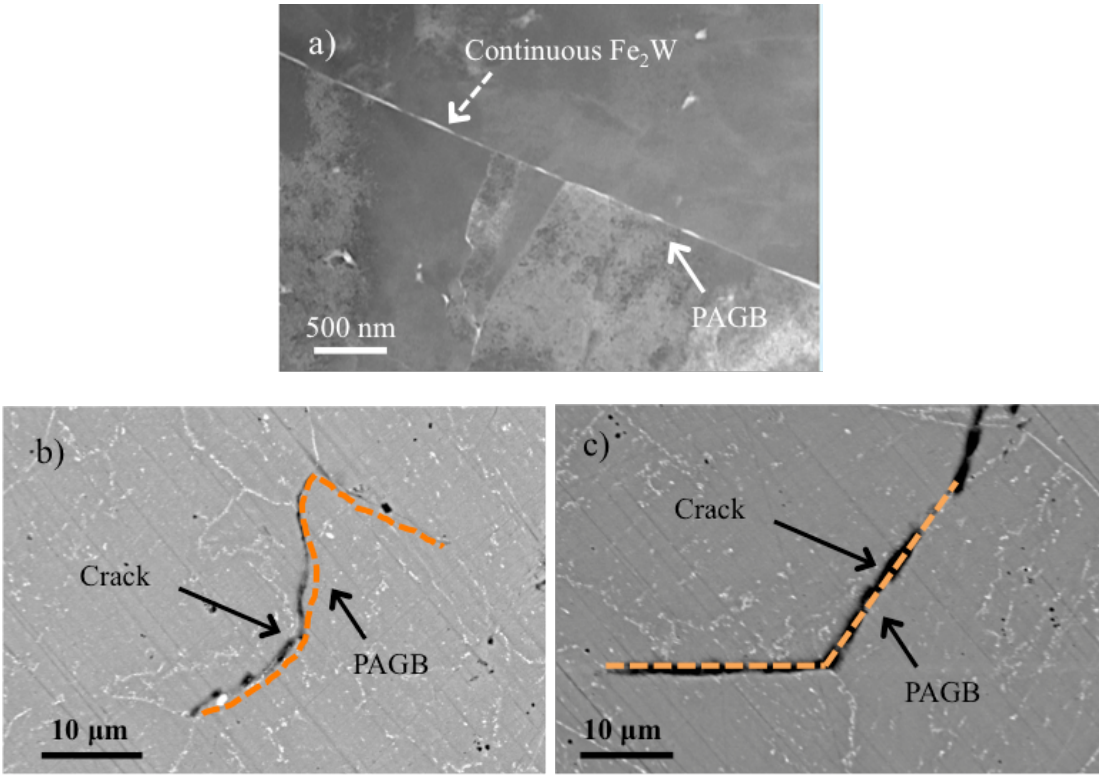

Figure 4.6 a) HAADF/STEM micrograph showing the continuous Laves-phase films at a PAGB in ZTa-ULC steel in the as-tempered condition, b and c) show the SEM/BSE micrographs taken from the longitudinal section of an impact-tested specimen of ZTa-ULC near the fracture surface.

Laves-phase precipitates are useful in the beginning of their formation, when they benefit from a fine distribution. However, they coarsen relatively quickly and form massive Laves-phase precipitates, which can lead to brittleness of 9–12% Cr steels. Thus, it is important to understand the precipitation behavior of Laves-phase and consequently impact toughness of Z-phase strengthened steels. Paper IV summarizes the effect of C and Cu on Laves-phase distribution and impact toughness and gives an insight to the effect of C on the precipitation of Ta-based Z-phase via comparing the ZTa-XHC and ZTa-ULC steels.

Besides the minor adjustment in the content of some of the alloying elements such Mn and Ni, aiming to balance the austenite/ferrite stabilizers, the alloy modification in ZTa-XHC compared to the ZTa-ULC steel involved two major changes: the addition of Cu and increasing the C content. ZTa-XHC was austenitized at 1150°C and cooled in air to room temperature. A special double-step tempering was designed for ZTa-XHC that aims at using the Cu precipitates that were formed in the first step as nucleation sites for Laves-phase. Besides, the removal of Cu from the matrix during the first step of tempering increases the A_{C1} temperature, allowing for a higher tempering temperature for the second step without forming reverse austenite. The double-step tempering was done at 650°C for 6 h followed by 6 h at 740°C or 700°C. Most of the microstructure investigations were done on the ZTa-XHC steel that was tempered at 650°C/6 h + 740°C/6 h and aged for 1000 and 5500 h at 650°C.

The addition of Cu and C resulted in the formation of Cu and $M_{23}C_6$ precipitates. The Cu precipitates are distributed at PAGBs, lath boundaries and within the laths. APT investigation on the matrix composition of the ZTa-XHC showed that most of the Cu content have precipitated during tempering treatment. The $M_{23}C_6$ precipitates were observed at the boundaries and within the laths in the as-tempered condition. The precipitation of Cu and $M_{23}C_6$ at PAGBs are the most important reasons to improve the distribution of Laves-phase in the form of equiaxed precipitates in ZTa-XHC compared to the continuous films at the boundaries in ZTa-ULC, see **Figure 4.7** and **Figure 4.6**.

The toughness of the ZTa-XHC steel in the as-tempered condition was evaluated using Charpy impact testing at room temperature and it was 76 J. The reason for such improvement in the impact toughness is due to the following reasons: precipitation of Cu and $M_{23}C_6$ at the boundaries, which occupy part of the boundary disturbing the formation continuous Laves-phase films, enhancing the nucleation of Laves-phase through increasing heterogeneous nucleation sites (Cu particles and $M_{23}C_6$ [98, 99]), decreasing the W content in the steel, and smaller PAG size of ZTa-XHC. **Figure 4.7 b** shows the presence of interrupted cracks within the matrix in the longitudinal section of an impact-tested specimen from ZTa-XHC.

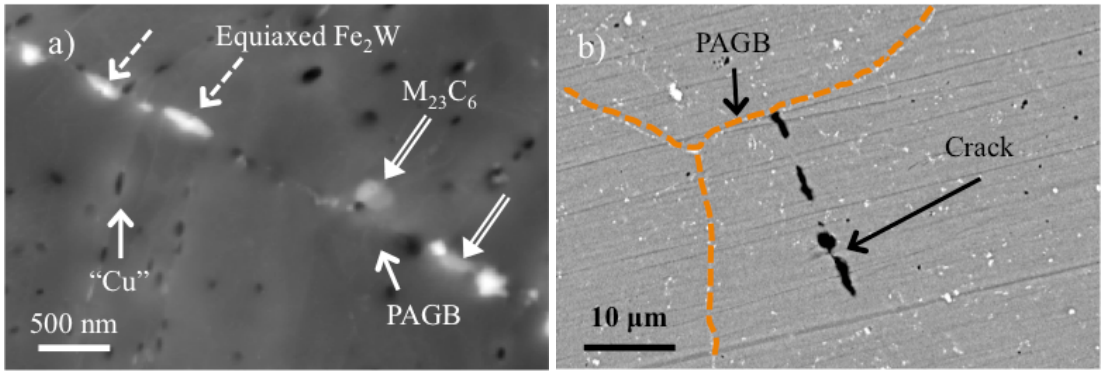

Figure 4.7 a) The presence of $M_{23}C_6$, Cu, and equiaxed Laves-phase at a PAGB in ZTa-XHC in the as-tempered condition, and b) the SEM/BSE micrographs taken from the longitudinal section of an impact-tested specimen of ZTa-ULC near the fracture surface.

4.4 The effect of carbon on Z-phase formation

Carbon plays a very important role in the precipitation behavior of steels. In the ZTa-XHC steel, the addition of C to the alloy affects the Z-phase formation in two ways: firstly, it consumes a fraction of the necessary alloying elements to form Z-phase, i.e. Cr, Ta, and N; secondly, it affects the chemistry of MX precipitates.

Addition of C leads to the formation of $M_{23}C_6$, TaC, and promotes the formation of BN inclusions. The formation of $M_{23}C_6$ consumes Cr, and hence the effective Cr content in the solid solution for Z-phase formation decreases. The formation of primary TaC consumes Ta, which was added to the steel with the purpose to form Z-phase. Part of the primary TaC particles do not dissolve during austenitization treatment, thus the Ta in these particles cannot contribute to the formation of Z-phase during tempering treatment or the early stages of the service.

The other primary particle formed in the ZTa-XHC is BN. B is a strong nitride former, and thus undesirable BN inclusions may form in 9–12% Cr steels containing both B and N. BN forms during the slow cooling process after solidification. The BN inclusions are detrimental not only due to consuming the beneficial alloying elements, but also due to their negative contribution to the mechanical properties. The presence of C increases the activity of B in the steel at the temperature range of 1050–1150°C and thus facilitates the formation of BN inclusions [65, 100].

The C addition also affects the chemistry of MX precipitates. The high C content in ZTa-XHC results in Ta(C, N) with varying ratio of C/N. As it is shown in **Figure 4.8**, the chemistry of a Ta(C, N) precipitate differs in the core and the shells of the precipitate. There is less C and higher N and Cr in the shells of the precipitate. This indicates that there is a high tendency for Ta(C, N) precipitates to dispose of C and take in Cr and N, which will eventually result in a transformation to Z-phase. The

experimental results show that TaN precipitates tend to contain much higher Cr content, which indicates that their transformation to Z-phase is much quicker than the transformation of Ta(C, N) precipitates to Z-phase. Hence the presence of C in steel and subsequently in MX decelerates the phase transformation from MX to Z-phase.

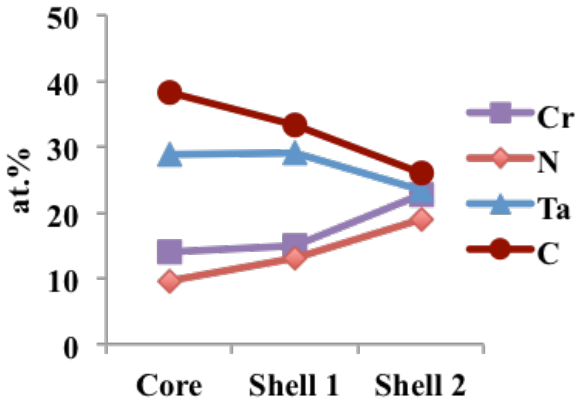

Figure 4.8 The composition of the core and shells of a Ta(C, N) in ZTa-XHC steel in the as-tempered condition.

In order to further investigate the role of C on the precipitation processes in Z-phase strengthened steels, in *Paper V*, a detail investigation was made on three trial steels, ZTa-LC (low carbon), ZTa-MC (medium carbon), and ZTa-HC (high carbon). The steels were studied by employing electron microscopy, APT, and XRD in the as-tempered condition and after ageing at 650°C. Steelmaking at Saarschmiede GmbH included vacuum induction melting and vacuum arc remelting, and ingots were forged to 40 mm × 40 mm square bars. The trial steels were then austenitized at 1100°C for 1 h, cooled in air to room temperature, and then double step tempered for 4 h at 650°C followed by 2 h at 750°C.

The effect of C content on the precipitation processes is discussed in two main sections of primary TaC precipitates and secondary Ta(C, N) precipitates.

Primary Ta-rich precipitates

In 9–12% Cr steels, the presence of primary particles, spherical MX particles, are important to hinder the coarsening of austenite grains during austenitization treatment via pinning the grain boundaries. However, as mentioned, these large primary Ta-rich particles consume a relatively high amount of Ta, which was added to the steels to form a fine distribution of secondary precipitates as strengthening agents.

In ZTa-LC, due to the low carbon content, almost no primary TaC is formed. However, some relatively large (a few hundred nanometer up to a micron) primary Z-phase particles were seen in the as-tempered condition, which remained in the

microstructure during ageing. In ZTa-MC and ZTa-HC steels, spherical TaC particles were formed. **Figure 4.9** shows the size distribution of primary TaC particles in ZTa-MC and ZTa-HC in the as-tempered condition. The obtained data was collected using Inca Feature Software in the SEM for particles larger than 80 nm. Higher amount and larger size of the primary TaC particles in ZTa-HC is a result of higher Ta and C contents in this steel compared to the ZTa-MC steel. Most of the primary TaC particles dissolved during ageing and are expected to increase the volume fraction of secondary precipitates. The presence of Z-phase precipitates in the form of elongated hexagons in the aged specimens, suggested that part of the smaller family of primary TaC could transform to Z-phase. A summary of the evolution of large and small primary Ta-rich particles is provided in the left and middle columns in **Figure 4.10**.

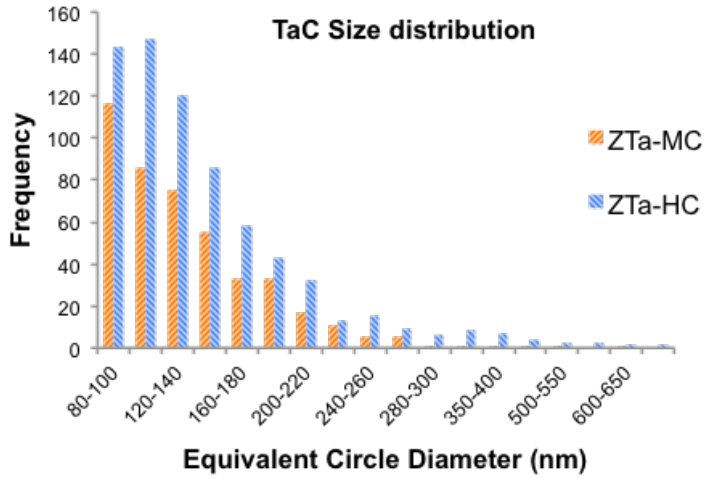

Figure 4.9 The size distribution of TaC particles collected from SEM/BSE micrographs for ZTa-MC (ZMC) and ZTa-HC (ZHC) in the as-tempered condition for particles bigger than 80 nm.

Secondary Ta(C, N) precipitates

The different C contents in the trial steels resulted in different C/N ratio in the secondary Ta(C, N) precipitates. APT data showed that the high C content in ZTa-HC caused a high C/N ratio in Ta(C, N) precipitates in the as-tempered condition. A lower C content resulted in a lower C/N ratio in the Ta(C, N) precipitates. The C/N ratio would at least partly (out-diffusion of C) control the rate of phase transformation from Ta(C, N) to Z-phase. The smaller C/N ratio in Ta(C, N) results in a faster transformation from MX to Z-phase, and hence a higher number density of Z-phase precipitates could be achieved during the early stages of ageing.

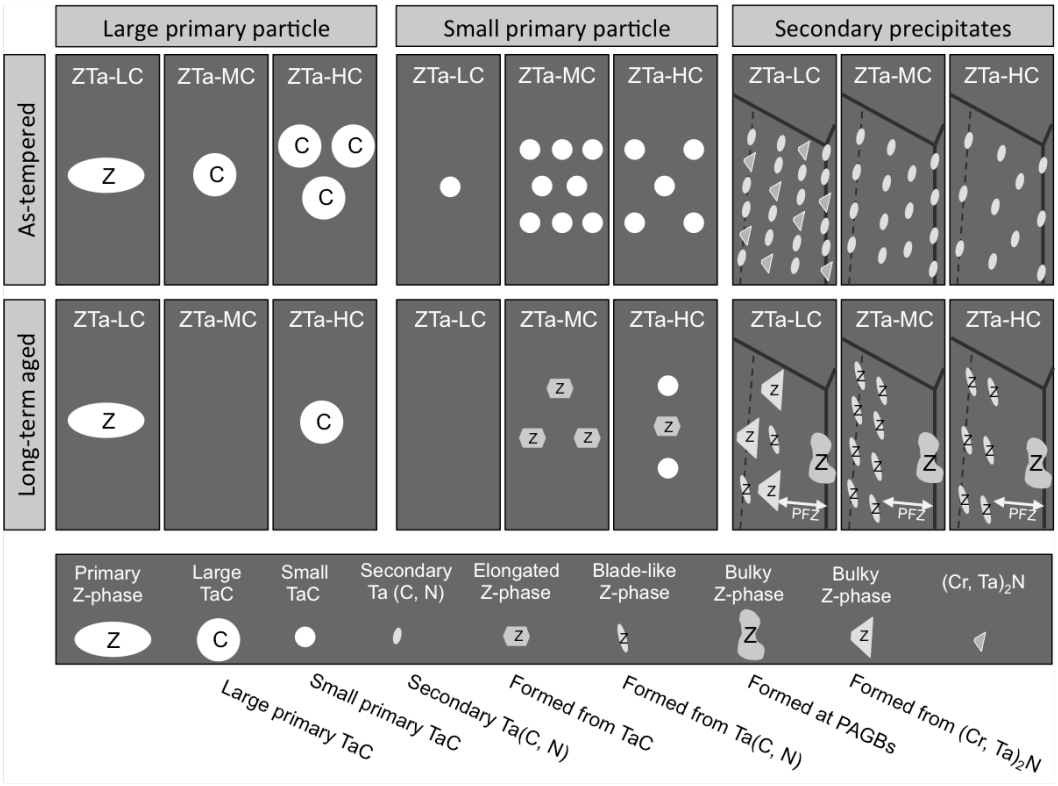

Figure 4.10 A schematic drawing of the microstructure evolution of Ta-rich particles in the trial steels. The full lines and dashed lines in the secondary precipitate column are PAGBs and lath boundaries, respectively.

4.5 Preferred mechanism to form Z-phase

A precipitation process is usually divided into three steps, nucleation, growth, and coarsening. Z-phase does not nucleate on its own and thus for an appropriate investigation on the precipitation behavior in Z-phase strengthened steels, one needs to consider the following four steps: nucleation of precursor phases (MX [77, 101] and M_2N [78]) to Z-phase, their transformation to Z-phase, growth, and coarsening. The main complication lies in the kinetics of the phase transformation and the growth steps, where the two phases MX and M_2N in principle independently and in reality in connection to each other transform to Z-phase. Thus the distribution of MX and M_2N, the kinetics of Z-phase formation from these phases, and the location of the precipitates, whether at high or low angle grain boundaries or within the matrix, can affect size, morphology, and their contribution to the strength of the steels.

MX to Z-phase transformation: APT and electron microcopy investigation showed that Ta(C, N), mainly with blade-like morphology, were nucleated at all grain boundaries as well as within the matrix. The transformation from MX to Z-phase is a continuous phenomenon, which includes in-diffusion of Cr from the matrix to the MX precipitates and out-diffusion of C from MX to adjacent $M_{23}C_6$ particles or to newly nucleated $M_{23}C_6$ particles. As a result of MX to Z-phase transformation, blade-like Z-

phase precipitates are formed that benefit from a fine distribution of precipitates at the boundaries and within the matrix.

Z-phase formation from M_2N: APT data showed that (Cr, Ta)$_2$N precipitates can contain up to 15 at. % Ta. This relatively high solubility of Ta in M_2N makes them a good nucleation site for a more stable nitride, Z-phase. Kim et al. [78] introduced a mechanism to form Z-phase from M_2N precipitates. As a consequence of a low carbon and high N contents in ZTa-LC, much more (Cr, Ta)$_2$N than Ta(C, N) formed in ZTa-LC in the as-tempered condition. After long-term ageing, a higher amount of bulky Z-phase were formed compared to the Z-phase of the blade-like morphology in ZTa-LC. This suggests that (Cr, Ta)$_2$N promotes the formation of bulky Z-phase. The less frequently seen blade-like Z-phase after long-term ageing in ZTa-LC could imply that Z-phase forms faster from (Cr, Ta)$_2$N and hence results in dissolution of part of the Ta(C, N) before they transform to Z-phase.

In short, in ZTa-LC, transformation from (Cr, Ta)$_2$N to Z-phase dominates and results in formation of large bulky Z-phase, which can lead to a dramatic loss in the strength of the steel. This suggest that for alloy design, the ratio between Ta, N, and C must be considered in such a way that formation of (Cr, Ta)$_2$N is avoided. A summary of evolution of secondary precipitates including MX and M_2N in ZTa-LC, ZTa-MC, and ZTa-HC is provided in **Figure 4.10**.

4.6 Combining Ta and Nb

Investigation of the ZNb-ULC and ZTa-ULC gave indications that the NbN precipitates transform faster to Z-phase compared to the TaN precipitates to Z-phase. However, the Ta-based Z-phase benefit from a denser distribution and slower coarsening rate than the Nb-based Z-phase. The precipitation behaviour for combined V and Nb has been investigated in the literature, for example by Lee et al. in Ref. [102] and Suzuki et al. in Ref. [103]. Combining V and Ta resulted in the precipitation of primary TaC and secondary (Ta, V)(C, N) [104]. However, experimental investigation of the precipitation process in the presence of both Ta and Nb has not been reported to the knowledge of the author. Based on a density functional theory study, Urban and Elsässer [105] reported that formation of a mixed Z-phase based on the combination of Nb and Ta is energetically favourable. Moreover, the idea with ZTaNb-MC steel was to study the Z-phase formation in the presence of combined Nb and Ta, and to investigate whether it is possible to combine the dense distribution of Ta-based Z-phase with the faster formation of Nb-based Z-phase, in order to achieve a better creep resistance.

The primary MX particles were of type TaC in ZTa-series of steel, while the presence of combined Nb and Ta, incorporates C, N, and B in the primary MX particles, (Ta, Nb)(C, N, B).

The secondary MX precipitates are of type (Ta, Nb)(C, N) with varying amount of Cr. The Nb/Ta ratio in the MX precipitates is lower than that of the Z-phase precipitates. The preliminary investigation on the ZTaNb-MC steel was reported in *Paper VI*. The combination of Nb and Ta to form Z-phase did not result to a fine distribution of Z-phase precipitates. However, further investigation on this trial steel can provide very valuable inputs to the understanding of the Z-phase formation and differences in the Ta and Nb to form Z-phase.

In *Paper VII*, a summary of the steps taken in the alloy development is provided through putting the trial steels in three series, referred to as S1, S2, and S3, out of which S3-2, S3-3, and S3-4 have not yet been investigated.

Chapter 5

Conclusions and outlook

Everything will be okay in the end!

If it is not okay, it is not the end…

John Lennon
An English singer-songwriter (1940-1980)

In this thesis, it was shown that depending on the precipitation processes, Z-phase can be used as strengthening phase rather than weakening phase to provide creep resistance at 650°C. A precipitation process is usually divided into three steps, nucleation, growth, and coarsening. Z-phase does not nucleate on its own and thus for an appropriate investigation on the precipitation behavior in Z-phase strengthened steels, one needs to consider the following four steps: precipitation of precursor phases (MX and M_2N) to Z-phase, the transformation from MX or M_2N to Z-phase, growth, and coarsening. The main conclusions on the steps are as follows:

Precipitation of precursor phases and Z-phase formation

Z-phase forms through a gradual transformation of existing MX and M_2N precipitates. In two model alloys, combining a high Cr content with N, Ta or Nb, and ultra-low carbon content (0.005 wt.%) resulted in formation of a fine distribution of TaN/NbN in the as-tempered condition, which transformed to Z-phase upon ageing.

As a result of the MX to Z-phase transformation, blade-like Z-phase precipitates were formed, which provided precipitation hardening to the steels. The model alloys, however, suffered from a low impact toughness due to the formation of continuous Laves-phase at boundaries in the absence of $M_{23}C_6$. We have shown that addition of Cu can provide heterogeneous nucleation sites for Laves-phase and hence an improved distribution of Laves-phase in the form of equiaxed particles was achieved. The formation of $M_{23}C_6$ also played a critical role to improve the distribution of Laves-phase at the boundaries.

Carbon plays a very critical role in both precipitation and transformation of precursor phases to Z-phase in Z-phase strengthened steels. Introducing varying amount of C to a series of trial steels showed that decreasing the C content in the steel leads to a lower C/N ratio in the Ta(C, N) precipitates and hence a faster transformation from MX to Z-phase. However, the low C content in the presence of excess N promoted the formation of (Cr, $Ta)_2N$ that transforms to large bulky Z-phase precipitates upon ageing, which do not contribute much to the precipitation hardening.

Growth step

The varying composition of MX in relation to Cr, C, and N contents due to ongoing dissolution/transformation of the precipitates resulted in a different kinetics amongst the MX precipitates to form Z-phase: the precipitates with higher Cr content and lower C/N ratio transform faster to Z-phase, and the adjacent Ta(C, N) precipitates can dissolve before they transform to Z-phase. This resulted in a fast growth period that led to a fine *enough* distribution of Z-phase precipitates to achieve creep resistance comparable to commercially available 9% Cr steels. Z-phase strengthened steels contain a higher Cr content and thus have better corrosion resistance. However, to improve also the creep resistance, we need to control the chemistry of MX precipitates so that if not all, but most of them transform to Z-phase and the high number density of MX is preserved after phase transformation.

Coarsening step

Both experimental and theoretical coarsening constants show that Ta-based Z-phase coarsens much slower than the Nb-based Z-phase during isothermal ageing at 650°C. The experimental coarsening constant is 2.8×10^{-31} (m^3s^{-1}) and 1.4×10^{-30} (m^3s^{-1}) for CrTaN and CrNbN, respectively. The measured coarsening rate for Ta-based Z-phase is comparable to that for VN precipitates that are responsible for long-term creep resistance of the best available 9% Cr steel, P92. It was also shown that even though Co is not directly involved in the Z-phase precipitates, it can decrease the coarsening rate of Z-phase via decreasing the diffusivity of Ta in the steel matrix.

Proposal to next series of Z-phase strengthened steels

Considering that the key alloying elements in the formation of Z-phase, Cr, N, Ta, and C, are also involved in other phases such as primary MX particles (TaC), BN inclusions, $M_{23}C_6$, Laves-phase, Ta-oxides, and Cr_2N, it is important to find the right balance between these elements so that the MX to Z-phase transformation is the dominant mechanism to form Z-phase. For the next series of trial steels, it is important to consider a higher Ta content to compensate for the portion of Ta that is bound to the large primary TaC. The C content must be limited to 0.02 wt.% in order to form secondary Ta(C, N) with a low C/N ratio. A low C content also limits the formation of large primary TaC, and hence more Ta is readily available for secondary precipitation. Such a low C content also limits the formation of $M_{23}C_6$, and thus, more Cr is left in the matrix resulting in a higher driving force to form Z-phase. A high N content does not necessary result in Ta(C, N) with a high N/C ratio, instead the excess N promotes the unfavorable M_2N precipitates, and thus the amount of N must be proportional to the *effective* Ta content (considering the loss of Ta to primary TaC, and Ta-oxides).

Moreover, Co was found to be beneficial for different reasons. First of all, a high Co content reduces the affinity of Cr in the matrix and hence a faster transformation from MX to Z-phase can be expected. Thus a high Co can increase the kinetics of Z-phase formation and hence higher possibilities to preserve the dense distribution of MX precipitates after transformation to Z-phase. Secondly, Co decreases the diffusivity of Ta within the steel matrix, and a slower coarsening rate can be expected in the presence of high Co content. The S3 series of steels in *Paper VII* are designed with higher Co and further investigation on this trial steels would reveal the optimized Co content.

The presence of large Z-phase precipitates at the PAGBs, and corresponding precipitate free zone adjacent to these large Z-phase precipitates indicates a faster formation of Z-phase at the PAGBs and dissolving the neighboring Ta(C, N) precipitates. This obviously results in a preferential recovery at the PAGBs and hence a dramatic decrease in the creep strength of the steel. Thus a high austenitization temperature, 1150°C, is recommended for the trial steels to allow sufficient austenite grain growth. Besides, austenitization at higher temperature leads to dissolution of large primary TaC and hence more Ta is available for secondary precipitation of precursor phases to Z-phase.

The presence of B at the Z-phase/matrix interface may also affect the coarsening behavior of Z-phase through altering the interfacial energy, which can be further investigated. Ta has a high affinity to oxygen and in almost all trial steels, large Ta-oxides were formed during steelmaking progress, which not only consumes Ta in an unfavorable manner but also results in a poor impact toughness of the trial steels.

Thus the oxygen level in all Ta-containing steels must be monitored in order to limit the Ta-oxide formation.

The Cu was found beneficial to improve the distribution of Laves-phase, and therefore 2 wt.% Cu is recommended for the next generation of Z-phase strengthened steels. Considering the very low C content, there will not be much help from $M_{23}C_6$ precipitates and thus the W content must be limited to 2 wt.% in order to avoid the formation of continuous films of Laves-phase at the boundaries and poor impact toughness.

Suggestions for further work

Within the Z-Ultra consortium, several large-scale demonstrations were completed that require microstructural investigation. For example, four tubes (42× 6×735 mm) were made from the ZTa-XHC steel and were installed in two power plants in Kiev. The tubes are now removed from the boilers and require microstructural investigation especially on the welded parts to study the precipitation behavior in the heat affect zone. Moreover, a large forging for turbine rotor part with 10–12 tonnes weight and a diameter around 1,100 mm, and a length of 1,600 mm was produced. The ZTa-MC steel was selected to produce the forging part. The forgeability of the steel was proved to be good and no severe cracks occurred during the forging. It also has a good machinability. There will be mechanical testing and a microstructure investigation should be made on the forged part.

We have also started to look into the effect of tempering on the creep resistance of the trial steels, and an investigation on ZTa-XHC steel with two tempering conditions has been initiated. The aim is to understand the effect of tempering temperature on the kinetics of Z-phase formation. For example, if a high dislocation density as a result of a low temperature tempering would enhance the Z-phase formation and a higher number density of Z-phase can be achieved, or the low tempering temperature enhances the formation of M_2N rather than MX. The chemistry of MX precipitates can also vary depending on the tempering temperature, and the question to answer is if we can get Ta(C, N) with a higher N/C so that phase transformation to Z-phase is accelerated. The size of precipitates can also vary depending on the tempering temperature, which should be investigated.

Acknowledgments

There are so many wonderful people to whom I am indebted to for their help and support during the years it has taken me to this point.

I would like to express my deep appreciation to my supervisors Associate Professor Fang Liu and Professor Hans-Olof Andrén for so many things but first of all giving me the opportunity to enjoy an adventurous life as a PhD student.

Hans-Olof, you are an incredible person, a brilliant material scientist, and unlimited source of knowledge in the field of microscopy and atom probe tomography. I would like to express my wholehearted gratitude to you not only for all the guidance you gave me on *Z-phase*, but also for all the lessons you taught me *via* Z-phase, on top of all, responsibility, caring, and cheerfulness! Coming to responsibility and our never ending discussions which sometimes continued up to evenings, I would also like to thank Gunvor for her patience and understanding.

It is with sincere gratitude that I wish to thank you Fang. You are a great example of a ***co***-supervisor (even when you became my main supervisor), spending so much time (*with a lot of patience*) teaching me from the basics of specimen preparation up to more advance details of operating electron microscopes and data evaluation of atom probe tomography. Thank you very much for your always-positive attitude, kindness, and support.

This work is done in a close collaboration with Professor John Hald from Technical University of Denmark, Lennart Johansson from Siemens Industrial Turbomachinery AB, Finspång, and Dr. Torsten-Ulf Kern, Siemens AG, Mülheim. I would like to express my deep appreciation to John for fruitful discussions and his valuable ideas and comments that led to a better understanding of the steels. Thank you Lennart for all the mechanical testing of the steels and the interpretation of the results, your years of experience in one of the best creep testing labs in the world provided valuable inputs to the work. I would also like to acknowledge Torsten for his valuable input during project meetings. To me, you are the most goal-oriented person I have ever met. While it is easy for me to get lost in the detail results from APT and TEM, you can easily put them into a much bigger perspective, reminding the *goal* of the project.

During the PhD period, I also got the opportunity of working together with wonderful people within the Z-Ultra consortium, and I would like to thank all the partners for their unique contribution to the understanding of Z-phase strengthened steels. I would like to specially acknowledge Professor Hermann Riedel from Fraunhofer Institute for Mechanics of Materials IWM for his great contribution as the project coordinator and organizing valuable workshops, and meetings. Hermann, it was always a pleasure talking to you.

My appreciation goes to all members of the Materials Microstructure and Eva Olsson Group divisions, for providing a very warm and friendly condition. I would like to thank Professor Krystyna Stiller and Professor Mats Halvarsson, the former and current head of M2 division, for all their effort to improve the working condition and their support during the years. Materials Microstructure division could not be any better! Special thanks goes to Professor Lena Falk for all the help with planning my PhD studies and an awesome course on TEM. Coming to the experiments, I must express my appreciation to Associate Professor Mattias Thuvander and Professor Mats Halvarsson for their great support on APT and TEM from tutorials to all "1-minute" questions. Continuing on the microscopes, I *seriously* thank Dr. Anders Kvist and Dr. Stefan Gustafsson for their always-good attitude and special *sense of humor*, as well as all the technical support on the microscopes. Special thank to Ola Löfgren for his support on all my Apple-related problems. I would also like to thank Kristina (my awesome office-mate), Silvia, Olof, Amine, Anand, Nooshin, Robert, Mohsen, Manfred and Gustav for all the friendship, support, fun games, and all our interesting discussions during lunchtime and fika.

My deepest and warmest appreciations go to my amazing parents, sister, and brothers for their infinite support, care, kindness, and love. Without your support, I could never make it. Thank you for believing in me, even when I doubted myself. Last but not least, I would like to thank my beloved wife, Somi, thank you very much for your patience and understanding, your endless love, care, kindness, and help. Your support during the years means a lot to me!

Masoud Rashidi
Gothenburg
Sweden
2017

References

[1] W. Heller, “Carbon dioxide storage - EU legal framework for carbon capture and storage,” *ATW - Int. Zeitschrift für Kernenergie*, vol. 53, no. 2008, pp. 599–644, 2017.

[2] F. Birol, “International Energy Agency,” *Key World Energy statistics*, 2017. [Online]. Available: www.iea.org/publication/KeyWorld2017.pdf.

[3] J. Hald, “High-alloyed martensitic steel grades for boilers in ultra-supercritical power plants,” in *Materials for ultra-supercritical and advanced ultra-supercritical power plants*, A. Di Gianfrancesco, Ed. Woodhead publishing, 2016, pp. 77–97.

[4] F. Masuyama, “History of Power Plants and Progress in Heat Resistant Steels,” *Iron Steel Inst. Japan Int.*, vol. 41, no. 6, pp. 612–625, 2001.

[5] F. Abe, “New martensitic steels,” in *Materials for ultra-supercritical and advanced ultra-supercritical power plants*, A. Di Gianfrancesco, Ed. Woodhead publishing, 2016, pp. 323–374.

[6] A. Di Gianfrancesco, “The fossil fuel power plants technology,” in *Materials for ultra-supercritical and advanced ultra-supercritical power plants*, A. Di Gianfrancesco, Ed. Woodhead publishing, 2016, pp. 1–24.

[7] S. Roberts, “Martensitic steels for cast components in ultra-supercritical power plants,” in *Materials for ultra-supercritical and advanced ultra-supercritical power plants*, A. Di Gianfrancesco, Ed. Woodhead publishing, 2016.

[8] A. Shibli, “Damage to coal power plants due to cyclic operation,” in *Coal Power Plant Materials and Life Assessment*, Woodhead Publishing Limited, 2014, pp. 333–357.

[9] T.-U. Kern and H. Almstedt, “Material and design aspects for modern steam power plants,” in *Advances in materials technology for fossil power plants proceeding from the eighth conference*, 2016, pp. 90–100.

[10] F. Masuyama, “Low-alloy steel grades for boilers in ultra-supercritical power plants,” in *Materials for ultra-supercritical and advanced ultra-supercritical power plants*, A. Di Gianfrancesco, Ed. Woodhead Publishing, 2016, pp. 53–76.

[11] F. Abe, “Development of creep-resistant steels and alloys for use in power plants,” in *Structural Alloys for Power Plants*, 2014, pp. 250–293.

[12] Y. Yin and R. Faulkner, “Physical and elastic behaviour of creep-resistant steels,” in *Creep-resistant steels*, F. Abe, T.-U. Kern, and R. Viswanathan, Eds. Woodhead publishing, 2008, pp. 217–241.

[13] J. Hald, “Microstructure and long-term creep properties of 9–12% Cr steels,” *Int. J. Press. Vessel. Pip.*, vol. 85, no. 1–2, pp. 30–37, 2008.

[14] G. Zeiler, “Martensitic steels for rotors in ultra-supercritical power plant,” in *Materials for ultra-supercritical and advanced ultra-supercritical power plants*, A. Di Gianfrancesco, Ed. Woodhead publishing, 2016, pp. 143–174.

[15] E. Basson, “www.worldsteel.org,” *World steel in figures 2017*, 2017. [Online].

Available: www.worldsteel.org.

[16] H. Bhadeshia and R. Honeycomb, *Steels, Microstructure and Properties*, 4th ed. Butterworth-Heinemann, 2017.

[17] M. E. Kassner and M.-T. Pérez, "Introduction," in *Fundamentals of creep in metals and alloys*, Elsevier Ltd, 2004, pp. 3–8.

[18] F. Abe, "Introduction," in *Creep-resistant steels*, F. Abe, T.-U. Kern, and R. Viswanathan, Eds. Woodhead publishing Limited, 2008, pp. 3–14.

[19] M. F. Ashby, "A first report on deformation mechanism maps," *Acta Metall.*, vol. 20, no. 7, pp. 887–897, 1972.

[20] H. Magnusson and R. Sandström, "Creep strain modeling of 9 to 12 Pct Cr steels based on microstructure evolution," *Metall. Mater. Trans. A*, vol. 38 A, no. 9, pp. 2033–2039, 2007.

[21] T. Shrestha, M. Basirat, I. Charit, G. P. Potirniche, and K. K. Rink, "Creep rupture behavior of Grade 91 steel," *Mater. Sci. Eng. A*, vol. 565, pp. 382–391, 2013.

[22] R. W. Warke, W. A. Bruce, D. J. Connel, S. R. Harris, M. Kuo, and S. J. Norton, "Carbon and low-alloy steels," in *Welding Handbook Volume 4, Materials and Applications*, American Welding Society, 2011, pp. 1–93.

[23] W. Yan, W. Wang, Y. Shan, K. Yang, and W. Sha, "Introduction to heat resistant steels," in *9-12Cr Heat- Resistant Steels*, Springer, 2015, pp. 1–27.

[24] M. Yoshizawa and M. Igarashi, "Long-term creep deformation characteristics of advanced ferritic steels for USC power plants," *Int. J. Press. Vessel. Pip.*, vol. 84, no. 1–2, pp. 37–43, 2007.

[25] K.-H. Mayer and F. Masuyama, "The development of creep-resistant steels," in *Creep-resistant steels*, F. Abe, T.-U. Kern, and R. Viswanathan, Eds. Woodhead publishing, 2008, pp. 15–77.

[26] X. Tao, J. Gu, and L. Han, "Carbonitride Dissolution and Austenite Grain Growth in a High Cr Ferritic Heat-resistant Steel," *Iron Steel Inst. Japan Int.*, vol. 54, no. 7, pp. 1705–1714, 2014.

[27] Y. Tanaka, "Production of creep resistant steels for turbines," in *Creep-resistant steels*, F. Abe, T.-U. Kern, and R. Viswanathan, Eds. Woodhead publishing, 2008, pp. 174–212.

[28] R. W. Swindeman, M. L. Santella, P. J. Maziasz, B. W. Roberts, and K. Coleman, "Issues in replacing Cr-Mo steels and stainless steels with 9Cr-1Mo-V steel," *Int. J. Press. Vessel. Pip.*, vol. 81, no. 6, pp. 507–512, 2004.

[29] F. Abe, "Strengthening mechanisms in steel for creep and creep rupture," in *Creep-resistant steels*, F. Abe, T.-U. Kern, and R. Viswanathan, Eds. Woodhead publishing, 2008, pp. 279–305.

[30] X. Z. Zhang, X. J. Wu, R. Liu, J. Liu, and M. X. Yao, "Influence of Laves phase on creep strength of modified 9Cr-1Mo steel," *Mater. Sci. Eng. A*, vol. 706, no. August, pp. 279–286, 2017.

[31] O. Prat, J. Garcia, D. Rojas, C. Carrasco, and G. Inden, "Investigations on the growth kinetics of Laves phase precipitates in 12% Cr creep-resistant steels: Experimental and DICTRA calculations," *Acta Mater.*, vol. 58, no. 18, pp.

6142–6153, 2010.

[32] M. Taneike, F. Abe, and K. Sawada, “Creep-strengthening of steel at high temperatures using nano-sized carbonitride dispersions,” *Nature*, vol. 424, no. 6946, pp. 294–296, 2003.

[33] H. Magnusson and R. Sandström, “The Role of Dislocation Climb across Particles at Creep Conditions in 9 to 12 Pct Cr steels,” *Metall. Mater. Trans. A*, vol. 38, no. 10, pp. 2428–2434, 2007.

[34] K. Maruyama, “Fundamental aspects of creep deformation and deformation mechanism map,” in *Creep-resistant steels*, F. Abe, T.-U. Kern, and R. Viswanatan, Eds. Woodhead publishing, 2008, pp. 265–279.

[35] H. K. Danielsen and J. Hald, “Influence of Z-phase on Long-term Creep Stability of Martensitic 9 to 12% Cr Steels,” *VGB PowerTech*, vol. 5, pp. 68–73, 2009.

[36] A. Kostka, K. G. Tak, R. J. Hellmig, Y. Estrin, and G. Eggeler, “On the contribution of carbides and micrograin boundaries to the creep strength of tempered martensite ferritic steels,” *Acta Mater.*, vol. 55, no. 2, pp. 539–550, 2007.

[37] D. Porter and K. Easterling, “Crystal interfaces and microstructure,” in *Phase transformation in metals and alloys*, Nelson Thrones Ltd, 1992, pp. 110–185.

[38] N. Q. Zhu, L. Lu, Y. L. He, L. Li, and X. G. Lu, “Coarsening of $M_{23}C_6$ Precipitates in an Fe-Cr-C Ternary Alloy,” *J. Iron Steel Res. Int.*, vol. 19, no. 9, pp. 62–67, 2012.

[39] Z. Yongtao, M. Lede, W. Xiaojun, Z. Hanqian, and L. Jinfu, “Evolution Behavior of Carbides in 2.25Cr-1Mo-0.25V Steel,” *Mater. Trans.*, vol. 50, no. 11, pp. 2507–2511, 2009.

[40] O. Prat, J. García, D. Rojas, J. P. Sanhueza, C. Camurri, J. Garcia, D. Rojas, J. P. Sanhueza, and C. Camurri, “Study of nucleation, growth and coarsening of precipitates in a novel 9%Cr heat resistant steel: Experimental and modeling,” *Mater. Chem. Phys.*, vol. 143, no. 2, pp. 754–764, 2014.

[41] F. Abe, T. Horiuchi, M. Taneike, and K. Sawada, “Stabilization of martensitic microstructure in advanced 9Cr steel during creep at high temperature,” *Mater. Sci. Eng. A*, vol. 378, no. 1–2 SPEC. ISS., pp. 299–303, 2004.

[42] V. Knežević, J. Balun, G. Sauthoff, G. Inden, and A. Schneider, “Design of martensitic/ferritic heat-resistant steels for application at 650 °C with supporting thermodynamic modelling,” *Mater. Sci. Eng. A*, vol. 477, no. 1–2, pp. 334–343, 2008.

[43] M. Hättestrand and H.-O. Andrén, “Boron distribution in 9–12% chromium steels,” *Mater. Sci. Eng. A*, vol. 270, no. 1, pp. 33–37, 1999.

[44] M. Hättestrand, M. Schwind, and H.-O. Andrén, “Microanalysis of two creep resistant 9-12% chromium steels,” *Mater. Sci. Eng. A*, vol. 250, no. 1, pp. 27–36, 1998.

[45] A. Aghajani, C. Somsen, and G. Eggeler, “On the effect of long-term creep on the microstructure of a 12% chromium tempered martensite ferritic steel,” *Acta Mater.*, vol. 57, no. 17, pp. 5093–5106, 2009.

[46] J. S. Lee, H. Ghassemi Armaki, K. Maruyama, T. Muraki, and H. Asahi, "Causes of breakdown of creep strength in 9Cr-1.8W-0.5Mo-VNb steel," *Mater. Sci. Eng. A*, vol. 428, no. 1–2, pp. 270–275, 2006.

[47] A. Czyrska-Filemonowicz, A. Zielińska-Lipiec, and P. J. Ennis, "Modified 9 % Cr Steels for Advanced Power Generation : Microstructure and Properties," *J. Achiev. Mater. Manuf. Eng.*, vol. 19, no. 2, pp. 43–48, 2006.

[48] O. Prat, J. Garcia, D. Rojas, G. Sauthoff, and G. Inden, "The role of Laves phase on microstructure evolution and creep strength of novel 9%Cr heat resistant steels," *Intermetallics*, vol. 32, pp. 362–372, 2013.

[49] K. Sawada, H. Kushima, and K. Kimura, "Z-phase Formation during Creep and Aging in 9–12% Cr Heat Resistant Steels," *Iron Steel Inst. Japan Int.*, vol. 46, no. 5, pp. 769–775, 2006.

[50] A. Di Gianfrancesco, S. T. Vipraio, and D. Venditti, "Long Term Microstructural Evolution of 9-12 % Cr Steel Grades for Steam Power Generation Plants," *Procedia Eng.*, vol. 55, pp. 27–35, 2013.

[51] H. Chilukuru, K. Durst, S. Wadekar, M. Schwienheer, A. Scholz, C. Berger, K. H. Mayer, and W. Blum, "Coarsening of precipitates and degradation of creep resistance in tempered martensite steels," *Mater. Sci. Eng. A*, vol. 511, pp. 81–87, 2009.

[52] K. Sawada, K. Suzuki, H. Kushima, M. Tabuchi, and K. Kimura, "Effect of tempering temperature on Z-phase formation and creep strength in 9Cr-1Mo-V-Nb-N steel," *Mater. Sci. Eng. A*, vol. 480, no. 1–2, pp. 558–563, 2008.

[53] R. Agamennone, W. Blum, C. Gupta, and J. K. Chakravartty, "Evolution of microstructure and deformation resistance in creep of tempered martensitic 9-12%Cr-2%W-5%Co steels," *Acta Mater.*, vol. 54, no. 11, pp. 3003–3014, 2006.

[54] H. K. Danielsen and J. Hald, "A thermodynamic model of the Z-phase Cr(V, Nb)N," *Calphad*, vol. 31, no. 4, pp. 505–514, 2007.

[55] W. O. Binder, "Symposium on the nature, occurence, and effects of sigma-phase," in *ASTM STP 110*, 1950, pp. 146–164.

[56] T. Sourmail, "Precipitation in creep resistant austenitic stainless steels," *Mater. Sci. Technol.*, vol. 17, no. 1, 2001.

[57] D. H. Jack and K. H. Jack, "Structure of Z-phase, NbCrN," *J. Iron Steel Inst.*, vol. 209, pp. 790–792, 1972.

[58] L. Karlsson, A. Henjered, H.-O. Andrén, and H. Nordén, "Composition and crystallography of nitride precipitates in an austenitic stainless steel containing niobium and vanadium," *Mater. Sci. Technol.*, vol. 1, pp. 337–343, 1985.

[59] H. K. Danielsen, J. Hald, F. B. Grumsen, and M. A. J. Somers, "On the Crystal Structure of Z- Phase Cr (V , Nb) N," *Metall. Mater. Trans. A*, vol. 37, no. September, pp. 2633–2640, 2006.

[60] V. Vodarek and F. Filus, "On the role of Z-phase in heat resistant steels," in *Metal 2011: the 20th anniversary year of the International Conference on Metallurgy and Materials*, 2011, pp. 1–6.

[61] E. Schnabel, P. Schwaab, and H. Weber, "Metallkundliche Untersuchungen an

Warmfesten Stahlen," *Stahl Eisen*, vol. 107, pp. 691–696, 1987.

[62] A. Strang and V. Vodarek, "Z-phase precipitation in martensitic 12CrMoVNb steels," *Mater. Sci. Technol.*, vol. 12, pp. 552–556, 1996.

[63] K. Sawada, H. Kushima, K. Kimura, and M. Tabuchi, "TTP Diagrams of Z Phase in 9–12% Cr Heat-Resistant Steels," *Iron Steel Inst. Japan Int.*, vol. 47, no. 5, pp. 733–739, 2007.

[64] N. Takahashi, T. Fujita, and T. Yamada, "Effect of Boron on Long Period Creep Rupture Strength of 12%Cr Heat Resisting Steel," *Tetsu-to-Hagane*, vol. 61, no. 9, pp. 2263–2273, 1975.

[65] F. Abe, "Effect of Boron on Microstructure and Creep Strength of Advanced Ferritic Power Plant Steels," *Procedia Eng.*, vol. 10, pp. 94–99, 2011.

[66] F. Abe, "Precipitate design for creep strengthening of 9% Cr tempered martensitic steel for ultra-supercritical power plants," *Sci. Technol. Adv. Mater.*, vol. 9, no. 1, p. 13002, 2008.

[67] E. Plesiutschnig, C. Beal, S. Paul, G. Zeiler, and C. Sommitsch, "Optimised microstructure for increased creep rupture strength of MarBN steels," *Mater. High Temp.*, vol. 32, no. 3, pp. 318–322, 2015.

[68] B. Xiao, L. Xu, L. Zhao, H. Jing, Y. Han, and Z. Tang, "Microstructure evolution and fracture mechanism of a novel 9Cr tempered martensite ferritic steel during short-term creep," *Mater. Sci. Eng. A*, vol. 707, pp. 466–477, 2017.

[69] Z. Liu, H. Bao, and Z. Chen, "G115 steel and its application for 600+ °C A-ULC-PP," in *Advances in materials technology for fossil power plants proceeding from the eighth conference, Eds J. Parker, J. Shingledecker and J. Siefert*,ASM Internationals, Materials Park OH, 2016, pp. 1011–1018.

[70] Z. Liu, "Status of the power industry in China and overall progress for A-USC technology," in *Advances in materials technology for fossil power plants proceeding from the eighth conference, Eds J. Parker, J. Shingledecker and J. Siefert*,ASM Internationals, Materials Park OH, 2016, pp. 24–34.

[71] L. Tan, X. Ren, and T. R. Allen, "Corrosion behavior of 9-12% Cr ferritic-martensitic steels in supercritical water," *Corros. Sci.*, vol. 52, no. 4, pp. 1520–1528, 2010.

[72] W. J. Quadakkers, J. Żurek, and M. Hänsel, "Effect of water vapor on high-temperature oxidation of FeCr alloys," *JOM*, vol. 61, no. 7, pp. 44–50, 2009.

[73] A. Sedriks, "Corrosion by hot gases and molten compounds," in *Corrosion of stainless steels*, John Wiley & Sons, 1996.

[74] V. Sklenička, K. Kuchařová, M. Svoboda, L. Kloc, J. Buršík, and A. Kroupa, "Long-term creep behavior of 9–12%Cr power plant steels," *Mater. Charact.*, vol. 51, no. 1, pp. 35–48, 2003.

[75] H. K. Danielsen and J. Hald, "On the nucleation and dissolution process of Z-phase Cr(V,Nb)N in martensitic 12%Cr steels," *Mater. Sci. Eng. A*, vol. 505, no. 1–2, pp. 169–177, 2009.

[76] S. Spigarelli, "Quantification of the effect of early microstructural degradation during creep of 9Cr-1Mo-NbV steels at 600°C," *Mater. Sci. Eng. A*, vol. 565, pp. 269–277, 2013.

[77] L. Cipolla, H. K. Danielsen, D. Venditti, P. E. Di Nunzio, J. Hald, and M. A. J. Somers, "Conversion of MX nitrides to Z-phase in a martensitic 12% Cr steel," *Acta Mater.*, vol. 58, no. 2, pp. 669–679, 2010.

[78] M. Y. Kim, S. M. Hong, K. H. Lee, W. S. Jung, Y. S. Lee, Y. K. Lee, and J. H. Shim, "Mechanism for Z-phase formation in 11CrMoVNbN martensitic heat-resistant steel," *Mater. Charact.*, vol. 129, no. February, pp. 40–45, 2017.

[79] S. H. Ryu and J. Yu, "A new equation for the Cr equivalent in 9 to 12 pct Cr steels," *Metall. Mater. Trans. A*, vol. 29, no. 6, pp. 1573–1578, 1998.

[80] H. K. Danielsen, P. E. Di Nunzio, and J. Hald, "Kinetics of Z-Phase Precipitation in 9 to 12 pct Cr Steels," *Metall. Mater. Trans. A*, vol. 44, no. May, pp. 2445–2452, 2013.

[81] D. H. Jack and K. H. Jack, "Invited review: Carbides and nitrides in steel," *Mater. Sci. Eng.*, vol. 11, no. 1, pp. 1–27, 1973.

[82] S. Yamasaki, M. Mitsuhara, and H. Nakashima, "Development of High-chromium Ferritic Heat-resistant Steels with High-nitrogen Addition," *etsu-to-Hagané*, vol. 103, no. 1, pp. 64–72, 2017.

[83] F. Liu and H.-O. Andrén, "Initial study on Z-phase strengthened 9-12% Cr steels by atom probe tomography," in *Materials for Advanced Power Engineering*, 2010, pp. 107–116.

[84] L. Helis, Y. Toda, T. Hara, H. Miyazaki, and F. Abe, "Effect of cobalt on the microstructure of tempered martensitic 9Cr steel for ultra-supercritical power plants," *Mater. Sci. Eng. A*, vol. 510–511, no. C, pp. 88–94, 2009.

[85] J. P. Sanhueza, D. Rojas, O. Prat, J. Garcia, R. Espinoza, C. Montalba, and M. F. Melendrez, "Precipitation kinetics in a 10.5%Cr heat resistant steel: Experimental results and simulation by TC-PRISMA/DICTRA," *Mater. Chem. Phys.*, vol. 200, pp. 342–353, 2017.

[86] A. Fedoseeva, E. Tkachev, V. Dudko, N. Dudova, and R. Kaibyshev, "Effect of alloying on interfacial energy of precipitation/matrix in high-chromium martensitic steels," *J. Mater. Sci.*, vol. 52, no. 8, pp. 4197–4209, 2017.

[87] L. Li, R. Maclachlan, M. A. E. Jepson, and R. Thomson, "Microstructural evolution of boron nitride particles in advanced 9Cr power plant steels," *Metall. Mater. Trans. A*, vol. 44, no. 7, pp. 3411–3418, 2013.

[88] J. Goldstein, D. Newbury, D. Joy, and C. Lyman, *Scanning Electron Microscopy and X-ray Microanalysis*. Springer, 2003.

[89] D. B. Williams and C. B. Carter, *Transmission Electron Microscopy: A textbook for materials science*. Springer, 2009.

[90] B. . Hatt, "X-ray analysis of metallic materials," in *Smithells metals reference book (7th edition)*, E. . Brandes and G. . Brook, Eds. Elsevier, 1992, pp. 1–44.

[91] J. O. Andersson, T. Helander, L. Höglund, P. F. Shi, and B. Sundman, "Thermo-Calc and Dictra, Computational tools for materials science," *Calphad*, vol. 26, pp. 273–312, 2002.

[92] "Thermo-Calc Software TCFE8 Steels/Fe-alloys database."

[93] "Thermo-Calc Software MOBFE3 Steels/Fe-alloys mobility database."

[94] O. Prat, J. Garcia, D. Rojas, C. Carrasco, and A. R. Kaysser-Pyzalla, "Investigations on coarsening of MX and $M_{23}C_6$ precipitates in 12% Cr creep resistant steels assisted by computational thermodynamics," *Mater. Sci. Eng. A*, vol. 527, no. 21–22, pp. 5976–5983, 2010.

[95] M. Hättestrand and H.-O. Andrén, "Influence of strain on precipitation reactions during creep of an advanced 9% chromium steel," *Acta Mater.*, vol. 49, no. 12, pp. 2123–2128, 2001.

[96] M. Hättestrand and H.-O. Andrén, "Microstructural development during ageing of an 11% chromium steel alloyed with copper," *Mater. Sci. Eng. A*, vol. 318, no. 1–2, pp. 94–101, 2001.

[97] J. Ågren, M. T. Clavaguera-Mora, J. Golczewski, G. Inden, H. Humar, C. Sigli, and Ågren, "Group 3: Application of Computational Thermodynamics to Phase Transformation Nucleation and Coarsening," *Calphad*, vol. 24, no. 1, pp. 41–54, 2000.

[98] M. I. Isik, A. Kostka, V. A. Yardley, K. G. Pradeep, M. J. Duarte, P. P. Choi, and D. Raabe, "On the nucleation of Mo-rich Laves phase particles adjacent to $M_{23}C_6$ micrograin boundary carbides in 12% Cr tempered martensite ferritic steels," *Acta Mater.*, vol. 90, pp. 94–104, 2015.

[99] K. Rodak, A. Hernas, and V. Vodárek, "Microstructural characterization of second phases in X10CrMoVNb9 and 12CrMoWCuVNb steels after long steam exposure time at 550°C," in *XV International Conference on Electron Microscopy", 15 – 18 September 2014, Cracow, Poland*, 2014, pp. 793–803.

[100] K. Sakuraya, H. Okada, and F. Abe, "BN type inclusions formed in high Cr ferritic heat resistant steel," *Energy Mater.*, vol. 1, pp. 158–166, 2006.

[101] M. Rashidi, H.-O. Andrén, and F. Liu, "Core-shell structure of intermediate precipitates in a Nb-based Z-phase strengthened 12% Cr steel," *Microsc. Microanal.*, vol. 23, no. 2, pp. 360–365, 2017.

[102] K. H. Lee, S. M. Hong, J. H. Shim, J. Y. Suh, J. Y. Huh, and W. S. Jung, "Effect of Nb addition on Z-phase formation and creep strength in high-Cr martensitic heat-resistant steels," *Mater. Charact.*, vol. 102, pp. 79–84, 2015.

[103] K. Suzuki, S. Kumai, Y. Toda, H. Kushima, and K. Kimura, "Two-phase Separation of Primary MX Carbonitride during Tempering in Creep Resistant 9Cr1MoVNb Steel," *Iron Steel Inst. Japan Int.*, vol. 43, no. 7, pp. 1089–1094, 2003.

[104] X. Xiao, G. Liu, B. Hu, J. Wang, and A. Ullah, "Effect of V and Ta on the precipitation behavior of 12%Cr reduced activation ferrite/martensite steel," *Mater. Charact.*, vol. 82, pp. 130–139, 2013.

[105] D. F. Urban and C. Elsässer, "Atomic defects and dopants in ternary Z-phase transition-metal nitrides Cr M N with M= V, Nb, Ta investigated with density functional theory," *Phys. Rev. B*, vol. 96, no. 10, pp. 1–11, 2017.